Accepted Manuscript

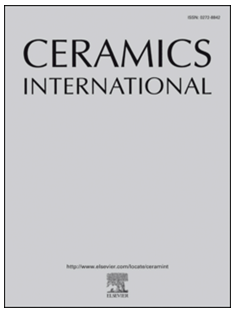

A holistic analysis of surface, chemical bonding states and mechanical properties of sol-gel synthesized CoZn-oxide coatings complemented by finite element modeling

M. Mahbubur Rahman, Ella Awaltanova, Amun Amri, Mohammednoor Altarawneh, Md Abul Hossain, Xiaoli Zhao, Willey Yun Hsien Liew, Manickam Minakshi, Chun Yang-Yin, Jean-Pierre Veder, Lee Siang Chuah, Zhong-Tao Jiang

PII: S0272-8842(19)30467-5

DOI: https://doi.org/10.1016/j.ceramint.2019.02.167

Reference: CERI 20890

To appear in: *Ceramics International*

Received Date: 25 January 2019

Accepted Date: 24 February 2019

Please cite this article as: M.M. Rahman, E. Awaltanova, A. Amri, M. Altarawneh, M.A. Hossain, X. Zhao, W.Y. Hsien Liew, M. Minakshi, C. Yang-Yin, J.-P. Veder, L.S. Chuah, Z.-T. Jiang, A holistic analysis of surface, chemical bonding states and mechanical properties of sol-gel synthesized CoZn-oxide coatings complemented by finite element modeling, *Ceramics International* (2019), doi: https://doi.org/10.1016/j.ceramint.2019.02.167.

A holistic analysis of surface, chemical bonding states and mechanical properties of sol-gel synthesized CoZn-oxide coatings complemented by finite element modelling

M Mahbubur Rahman[1,2*], Ella Awaltanova[1,3], Amun Amri[3], Mohammednoor Altarawneh[1], Md Abul Hossain[2], Xiaoli Zhao[4], Willey Yun Hsien Liew[5], Manickam Minakshi[1], Chun Yang-Yin[6], Jean-Pierre Veder[7], Lee Siang Chuah[8], Zhong-Tao Jiang[1*]

[1] Surface Analysis and Materials Engineering Research Group, School of Engineering & Information Technology, Murdoch University, Perth, WA 6150, Australia
[2]Department of Physics, Jahangirnagar University, Savar, Dhaka 1342, Bangladesh
[3]Department of Chemical Engineering, Universitas Riau, Pekanbaru, Indonesia
[4]School of Engineering, Edith Cowan University, Joondalup, WA 6027, Australia
[5]Faculty of Engineering, Universiti Malaysia Sabah, Jalan UMS, 88400, Kota Kinabalu, Sabah, Malaysia
[6]Newcastle University in Singapore, 537 Clementi Road #06-01, SIT Building @ Ngee Ann Polytechnic, Singapore 599493
[7]John de Laeter Centre, Curtin University, Perth, Western Australia 6102, Australia
[8]Department of Physics, School of Distance Education, Universiti Sains Malaysia, 11800 Minden, Penang, Malaysia

*Corresponding author: Z.Jiang@murdoch.edu.au; and M.Rahman@Juniv.edu

ABSTRACT

This article presents a comprehensive study on surface chemical bonding states, morphological features, mechanical properties, finite element modeling, and water contact angle measurements of wet chemical based dip-coated CoZn-oxide thin film coatings. Atomic force microscopy (AFM), X-ray photoelectron spectroscopy (XPS), Nanoindentation, finite element method (FEM) modeling, and drop shape analysis techniques were used to carry out the detailed measurements. AFM studies showed that the surface roughness values of all the coatings sturdily increased with the increase in sol concentrations. The gradual increase in sol concentrations and annealing temperature also had a remarkable influence over the Co-, and Zn-contents of these coatings given by XPS analysis. The deconvolution of Co $2p_{3/2}$ photoelectron lines revealed the

formation of $Co(OH)_2$, CoO, Co_2O_3, and Co_3O_4 phases from the coatings surface while low intensity satellite peaks developed due to a partial spinel lattice structure of Co-ions. The occurrence of Co_3O_4, CoO, and ZnO phases were also confirmed from the deconvolution of O 1*s* photoelectron lines. The elastic modulus, *E*, of CoZn-oxide thin film coating, varied within the range of 43.7– 69.2 GPa was comparable with that in CoCuO thin film coatings. The maximum stress level induced was estimated to be in the range of 4.0 – 6.5 GPa. However, as the thickness of the coatings is increased, the maximum stress level slightly decreased. The coatings were moderately hydrophobic.

Keywords: Sol-gel technique; CoZn-oxide coatings; nanoindentation,; Young's modulus; elastic constant; finite element method

1. Introduction

Nanosized transition metal oxide based thin coatings and other systems demonstrate a good combination of novel and unique chemical, electrical, magnetic, and physical properties which make them ideal candidates to be used as various functional and smart materials [1, 2]. These materials have good potential in numerous industrial applications, such as optoelectronics, magnetic memory devices, photo-catalysts, and gas sensors [3-7]. For instance, due its safe nature, cost-effectiveness, thermal stability, large band-gap (3.37 eV), ease control of particle morphology, simplicity of crystallization, and high electron mobility, ZnOs are widely used as substitutes for other metal oxides in the area of sensors, catalysts, solar energy materials, and magnetic applications [8-10]. As a result, they have received widespread attention within the scientific community [11-13]. Likewise, Co_3O_4 also has also applications in various fields such as heterogeneous catalysis, electrochromic devices, gas sensors, biosensors, supercapacitors, and lithium ion batteries [7, 14-16]. Over the years, efforts have been made to investigate Co_3O_4 structures due to their fascinating structural, electrical, chemical, electronic, mechanical, optical, photo-chemical, and magnetic properties [17, 18]. Co_3O_4, a direct band-gap semiconducting oxide has been extensively used as catalysts, Li-ion batteries, gas sensors, supercapacitors, energy storage and energy conversion devices, thin film materials, solar selective surfaces, drug deliveries, and magneto-optic recording media [19, 20].

In recent years, transition metals (*i.e*., Mn, Ni, Cu, and Co) doped ZnO semiconducting structures have been thoroughly investigated for their optical, photoluminescence, magnetic, and semiconducting properties due to their potential applications in magneto-optic, electronics, optoelectronics, microwave, and spintronic devices [21-25]. More recent studies show that Co-doped ZnO systems have gathered considerable research attention due to their extraordinary structural, chemical, magnetic, and optical properties and large number of favorable applications [26-28]. Annealing effects on the micro-structural and electrochemical features of sol-gel dip coating derived Al-incorporated CoZnO thin film coatings were studied by means of XRD, UV-Vis-NIR, and VSM techniques [29]. Optical studies indicated that the band-gap of Al-incorporated CoZnO films dropped from 3.99 to 3.83 eV with the rise in annealing temperature. The ferromagnetic characteristics of the films were also increased upon annealing. The structural and magnetic properties of transition metals such as Mn, Ni, and Cu doped CoZnO nanoparticles were systematically investigated [30]. Single phase hexagonal wurtzite structure of the nanoparticles was confirmed *via* XRD tests while the nanoparticle size was in between 25.3, and 33.5 nm. The ferromagnetic behaviour of the nanoparticles indicated strong exchange interactions between the delocalized carriers and the localized *d* spins of doped metals.

Magnetic and photocatalytic analysis of Co_3O_4-ZnO nanocomposites with an average particle size of 10-40 nm, synthesized using chemical process was conducted by magnetization measurements with variations in external magnetic fields and temperatures. Fast alignment of the magnetic moments of Co_3O_4-ZnO nanocomposites seen below ~15 K is associated with the interfacial polarizations while the photocatalytic activity of the nanocomposite systems was ascribed to the ability of charge separation and charge transfer mechanisms [31]. Nanostructured Co_3O_4/ZnO catalysts identified as $CoZnO_T$, $CoZnO_S$, and $CoZnO_P$ were studied for their physicochemical and catalytic properties [32]. The catalytic performance of Co_3O_4/ZnO nanoparticles were significantly enhanced from the pure oxide precursors. The HR-TEM studies also confirmed that the synthesis temperature strongly affects the particle morphology of the Co_3O_4/ZnO nanoparticles. Compared to the pure oxides, Co_3O_4/ZnO catalysts also required higher catalytic decomposition temperatures. Microwave applications, of Co/ZnO nanocomposites, in isolators and circulators were reported in another study [33]. Co/ZnO nanocomposites, formed by mixing Co nanoparticles and ZnO nanoparticles, did not show the off-diagonal component of magnetic permeability, however, higher magnetic coercivity and

saturation magnetization values were observed. The magnetic behaviors of nanostructured Co/ZnO were assumed to be related to the magnetic anisotropy of Co particles.

Theoretical investigations on the magnetic properties of CoZnO materials, using the Heisenberg exchange-coupling model, reported that the particles' size and shape play significant roles in controlling the magnetic behavior and magnetization phenomena [34]. The phase characteristics and optoelectronic applications of these materials were also discussed in terms of the diluted magnetic semiconducting systems. Extensive studies on these materials have also been carried out in search of their potential applications in solar energy harvesting, optoelectronic devices, synthetic and inorganic chemistry, and ultrasensitive detection [35, 36]. The influence of applied potentials on the particle morphology, physical features, and conduction properties of CoZnO nanotubes is also available in the literature. Higher potential difference results to a reduction in oxygen content and increase in crystallinity in the nanostructures, in combination with a change in their phase compositions. The crystalline features of the nanostructures and their conductivity, increased with the diminution of impurities [37]. CoZnO coatings deposited *via* sol-gel dip coating process onto the glass substrates were studied to reveal their optical, and magnetic properties in relation with the structural information [38]. XRD studies confirmed their crystalline behavior and wurtzite structure. SEM imaging established the porous surface of the coatings and the saturation magnetization gradually increased with the applied external magnetic field. An optical band gap of 3.55 eV was computed from the UV-Vis spectroscopic studies while the ferromagnetism of the coatings was detected in VSM studies. Metal doped ZnO, and ZnCoO single phase thin film coatings manufactured using spray pyrolysis process were analysed *via* XRD, SEM, and transmittance spectroscopy. Structural investigations indicated the hexagonal wurtzite structure with an average particle size of 19 to 25 nm. The experimental transmittance data perfectly fits with the theoretical calculations. The Levenberg–Marquardt least square method in combination with the Wemple– DiDomenico model were utilized to understand the electronic transition, optical absorption coefficient, and Tauc–Urbach theory [39].

The photovoltaic and photoconductive nature of CoZnO systems deposited onto the glass and silicon substrates were studied by Soylu *et al*. [40]. Authors have suggested that CoZnO systems deposited onto silicon substrates can be used as photodetectors. It was also reported that Co-doped ZnO shows higher absorption of the visible lights by forming hybrid O2*p* conduction band at lower band-gaps. In another study, the weak ferromagnetic behaviour of Co_3O_4-ZnO

nanoparticles was detected at a low temperature [41]. By adopting a suitable synthesis method, one can regulate the structural, chemical and surface morphology, and particle size of a material to be used in the desired technical applications. Nowadays, numerous methods are available to synthesize mixed metal oxide based thin film coatings or nanoparticle structures namely, hydrothermal process, chemical co-precipitation route, laser deposition method, polyol process, thermal decomposition method, electrochemical method, microwave assisted technique, standard ball milling scheme, sol-gel dip coating or spin coating procedure, and thermal evaporation approach [42-49]. The majority of these synthesis methodologies, generally, require complicated working procedures, higher reaction temperatures, high cost machineries, higher energy consumption, longer reaction times, and harmful and toxic organic reagents. In addition to these, their performance outcome may also hinder from the application viewpoint. In view of these facts, sol-gel spin coating method is considered to be one of the most convenient, simple, lucrative, environment friendly, and useful technique to synthesize metal oxide based thin film coatings together with an easy control of particle morphology. Thus in this study, CoZn-oxide thin film coatings with high purity level has been produced *via* sol-gel spin-coating method at various sol concentrations and annealing temperatures in a relatively shorter synthesis time. Moreover, even though many literature on the studies of structural properties, optical analysis, magnetic properties, physicochemical and catalytic properties of such coatings are available however a comprehensive study in regards to their surface morphological features, chemical bonding states, mechanical properties, and water contact angle analysis is yet to be conducted. Detailed characterizations of the synthesized coatings were carried out by AFM, XPS, nanoindentation, FEM and water contact angle studies.

2. Experimental

2.1 Thin film fabrication

Cobalt nitrate hexahydrate ($Co(NO_3)_2.6H_2O$; Merck, >99%), zinc nitrate trihydrate ($Zn(NO_3)_2.3H_2O$; Merck, >98.5%), propionic acid (C_2H_5COOH, Merck, >99%), and absolute ethanol (C_2H_5OH; Merck, >99%) were used as the raw materials to synthesize the spin-coated thin films. Commercial grade reflective aluminum sheets (Anofol, 2×4 cm^2) were used as substrate materials. The substrates were prepared by cleaning in a hot (85 °C) mixture of Cr(VI)-

oxide and H_3PO_4 for 10 minutes. Finally, the substrates were washed out in warm deionized water and dried up by flowing nitrogen gas flushes.

Appropriate amount of cobalt nitrate hexahydrate, and zinc nitrate trihydrate were dissolved in absolute ethanol. 0.3M C_2H_5COOH was used as the complexing agent to the solution, and a hotplate magnetic stirrer was used for 2 hours at a spin speed of 450 rpm to make a homogeneous solution. The resultant solution was used to synthesize the copper zinc oxide thin film coatings by using a spin coating machine. During the synthesis process, the substrate was rotated at a speed of 3000 rpm for 50 s, and the coated substrate was dried on a hotplate at 150 °C for 60 s. The entire process was repeated several times to achieve the desired film thickness. The final products were annealed at 400, 500, and 600 °C temperatures for 2 hours in air at a heating rate of 50 °C/min. The thin film coatings produced with a precursor concentration of 0.3M and annealed at 400, 500, and 600 °C temperatures were termed as S1, S2, and S3 respectively. The similar procedure was repeated to synthesize another two series of thin film coatings by varying the precursor concentrations to 0.5M, and 0.7M; and annealing temperatures 400, 500, 600 °C. These two series of samples were identified to be S4, S5, and S6; and S7, S8, and S9 respectively. A total of nine samples were investigated to complete this study.

2.2 AFM imaging

A high resolution atomic force microscopy (AFM Bruker, Dimension Edge) machine was employed for surface morphological study. The images were acquired in tapping mode at a tapping signal of 2.9 V, at room temperature. A rectangular cantilever was involved for collecting the AFM micrographs. In the scan control panel, following default set parameters were used in tapping mode operation; scan size: 5 µm, scan rate: 1 Hz, samples/line: 256. AFM images were analyzed using a LabVIEW computer software.

The three key parameters namely, the mean surface roughness, R_a, rms value of surface roughness, R_q, and *z* scale were estimated from the AFM micrographs. The mean surface roughness, R_a of a thin film materials can be calculated using [50],

$$R_a = \frac{\sum_{i=1}^{N} |h_i - \bar{h}|}{N} \quad (1)$$

where h_i is the roughness value of the coating at a point 'i', $\bar{h}$ indicates the mean roughness value, and N is the total data points counted for the imaging process. The rms value of surface

roughness, R_q measures the height deviations originated from the mean data plane and is described by the following formula [50],

$$R_q = \sqrt{\frac{\sum_{i=1}^{N} |h_i - \bar{h}|^2}{N}} \quad (2)$$

The *z* scale value provides with the vertical distance between the peak and bottom point through of an AFM image [51].

2.3 XPS measurements

XPS, a very powerful and popular tool extensively used in surface science to analyze the surfaces, and local electronic, and chemical bonding structures of various solids including thin film based materials. It is also utilized to examine the influence of defects on the electronic behaviors of materials. Chemical analysis of the coatings was performed via Kratos Axis-Ultra photoelectron spectrometer. The Kratos XPS machine uses Al-K_α monochromatic X-ray source with beam energy of 1486.6 eV at a power of ~10 mA and ~15 kV. Square size samples (2 mm × 2 mm) were mounted onto steel sample holder. A uniform pressure of 2.9×10^{-9} Torr was maintained in the XPS test chamber. The Cu 2*p*, Co 2*p*, O 1*s*, C 1*s* photoelectron lines were recorded with a 2D delay line detector. The photoelectron energy scale was calibrated using C1*s* (hydrocarbon; C–H) line–at 284.6 eV. CASA-XPS v.2.3.15 software was used for XPS data analysis and deconvolution of the curves. In order to avoid the possible charge shift, all XPS spectra were calibrated with respect to the C 1*s* peak at a binding energy of 284.6 eV.

2.4 Nanoindentation and FEM Modeling

An Ultra-Micro Indentation System 2000 workstation (CSIRO, Sydney, Australia) has been used in this work to investigate the mechanical properties of CoZn-oxide thin films. The nanoindentations system, is equipped with a diamond Berkovich indenter, which was calibrated using a standard fused silica specimen [52]. In order for the indentation depth to be kept below 10% of the film thickness, the load control method was used with a maximum loading of 200 □N. The setting of test points was 15 for loading and 20 for unloading. A more detailed description of the nanoindentation procedures can be found elsewhere [53, 54].

Comsol Multiphysics software [55] was used in this work for the simulation of the intensity and distribution of load induced stress within various film materials, thicknesses and substrates. Here the "load induced stress", referring to an artificial load during the modelling process to evaluate the load carrying capability of the coating layer, is adapted to differentiate from "residual stress", which is the remnant stress gained during the spattering process. Similar to our previous works [54, 56] a 2D axial symmetry model was incorporated, with a spherical indenter (5 µm radius) at the top of the film layer with different composition and thickness. The film layer was set at the top of two different types of substrate, aluminium and silica glass, which are typical for real industrial applications. Further details of FEM modeling, such as geometry, boundary conditions, and mesh generation, have been provided in our previous works [57, 58].

2.5 Contact angle measurements

Contact angle measurements were performed at ambient temperatures using an FTA1000 Drop Shape Analysis instrument (B Frame System, First Ten Angstroms, Virginia, USA) equipped with an automated dispensing syringe and a computer-controlled title stage. Water droplets of 5 µL were dispersed onto fabricated samples. The contact angles were obtained by analyzing the sessile drop images using Drop Shape Analysis software affiliated with the instrument. Three drop tests were performed on each sample and the average angle was adopted for wetting characterization.

3. Results and discussion

3.1 AFM analysis: surface morphology

Surface structural features and surface roughness values of CoZn-oxide thin film coatings studied using AFM system are shown in Figure 1. The surface roughness parameters of these coatings estimated *via* AFM imaging were delineated in Table 1. From Table 1, higher mean surface roughness and rms surface roughness values of CoZn-oxide coatings were observed at lower annealing temperatures. However, as the sol concentrations were enhanced the R_a and R_q values intensely increased from 35.4 to 84.4 nm, and from 43.9 to 109 nm, respectively within a mean image surface area of 58.6 μm^2. Thus, the annealing and concentration level of the

solutions used to synthesize the thin film coatings have significant affect the surface morphological features of these films. Higher sol concentrations initiate grain growth at the coating's surface and improves the surface roughness of the thin films. At higher sol concentration, due to material densification, finer grains growth along a *z*-direction, and perpendicular to the base material which resulted in higher ionic mobility. As a consequence of these effects, the surface roughness values of CoZn-oxide coatings became enlarged. At higher annealing temperatures, the atoms have adequate activation energy to occupy the correct site around the crystal lattice.

3.2 XPS analysis: chemical composition and electronic structure

The XPS measurements were performed to investigate the surface chemical composition of the CoZn-oxide thin film coatings and corresponding chemical bonding states of the constituent elements. The elemental atomic percentages of CoZn-oxide thin film coatings estimated *via* XPS survey scans conducted in the binding energy range of 0-1200 eV are displayed in Figure 2. The high resolution XPS spectra were calibrated with respect to the C1*s* spectra considered to be at a binding energy position of 284.6 eV. It is noted that all the XPS spectra acquired at different sol concentration and annealing temperatures were very similar to each other while the individual elemental core level peak positions own varied peak intensities. From Figure 2, it is seen that all the XPS spectra exhibited peaks associated to Co, Zn, and O elements present in the thin film coatings together with carbon peaks [59]. The atomic compositions of these coatings assessed from XPS scans are registered in Table 2. It is seen that annealing and sol concentrations have noticeable influence on the atomic compositions of these coatings. The Co and Zn-contents gradually increased with the subsequent increase in sol concentration up to 0.5M and then decreased at 0.7M. It was also noticed that as the annealing temperature rises the atomic contents of Co and Zn also steadily enhanced. Thicker and larger oxide layers of these coatings were observed to be predominant at higher sol concentrations and around the films surface.

The decoupling of high resolution Co2$p_{3/2}$ XPS spectra and its satellite, at various annealing temperature and sol concentrations, of CoZnO thin film coatings are presented in Figure 3. The curve fitting results of the deconvoluted high resolution XPS spectra along with the binding energy positions and component percentiles, representing various surface bonding states, of

CoZn-oxide coatings are set out in Table 3. Figure 3 indicates that the surface bonding features of Co2$p_{3/2}$ photoelectron lines are occupied within 778.45–787.21 eV. It was also observed that annealing at higher temperature does not alter the bonding structures of Co2$p_{3/2}$ photoelectron lines. However, higher sol concentrations result in the dominant occurrence of $Co(OH)_2$ phase at 780.18–783.21 eV and diminishing other possible phases such as CoO, Co_2O_3, Co_3O_4. The appearance of a satellite peak at above 786 eV confirms the occurrence of Co^{2+} ions. It is also assumed that the reasonably low intensity of these satellite peaks is due to a partial spinel lattice structure of Co-ions which may originate from a combination of Co(III) and Co(II) ions [60]. The majority of the satellite peaks originate from the cobalt oxide structure known to be Co_2O_3 phase while for samples S4 and S6 another additional cobalt oxide phase of Co_3O_4 was also detected. The first deconvolution curves of Co2$p_{3/2}$ photoelectron lines recorded at 778.45-781.09 eV are due to the octahedral phase of Co(III) ions known to be Metal $Co/Co_2O_3/CoO/Co_3O_4/Co(OH)_2$ phase. The second decoupling curves seen at 780.38-783.21 eV are assumed to be the tetrahedral contribution of Co(II) ions, generally giving out $Co_2O_3/Co_3O_4/Co(OH)_2$ phase.

The high resolution XPS spectra of Zn2*p* photoelectron lines of CoZn-oxide thin coatings before deconvolution and after deconvolution, are presented in Figures 4 and 5 comprise a doublet structure. The local environments of Zn, given by the XPS spectra of Zn2*p* photoelectron lines, did not indicate any significant tendency of shifting either towards the higher or lower energy sides due to the annealing or sol concentration effects [61]. The Zn2$p_{3/2}$ XPS spectra of these coatings, after curve fitting, were resolved into two components. The first component, seen at a range from 1021.47 to 1022.13 eV, can be allocated to metal Zn or Zn–O bonds [62]. The second component located at a binding energy range of 1022.36 to 1023.10 eV is ascribed to the Zn-O bonds. The binding energies of Zn2$p_{3/2}$ and Zn2$p_{1/2}$ photoelectron lines corresponding to 1021.9 and 1045.0 eV, respectively were due to the spin orbit coupling. The separation between Zn2$p_{3/2}$ and Zn2$p_{1/2}$ levels was found to be 23.1 eV which is comparable with the valance band width. This doublet peak energy separation is in good agreement with the standard reference values of 23.1 eV associated to Zn^{2+} ions [63]. Further observations confirmed that the ratio area occupied by Zn2$p_{3/2}$ and Zn2$p_{1/2}$ peaks was 2:1.

All the O1s spectra of CoZn-oxide thin film coatings can be deconvoluted into three Gaussian fitting curve components together with the existence of a shoulder at above 530.0 eV. Figure 6

presents the deconvolution of high resolution O1*s* XPS photoelectron lines of CoZn-oxide thin film coatings deposited at various annealing temperatures and sol concentrations. The deconvolution of high resolution of O1*s* XPS spectra promulgate three components together with the existence of a shoulder above 530.0 eV. The first fitting components seen within the binding energy range of 529.82–530.83 eV (purple) is recognized to O^{2-} ions resulting to either Co_3O_4, and/or CoO, and/or ZnO phase. The second decoupling components detected at 530.7–532.07 eV (pink) is considered to have arisen from OH-like species and/or O^{2-} ions, and thereby producing Co_3O_4, and/or ZnO, and/or $Co(OH)_2$ phase [64-66]. The second components are, typically, related to the occurrence of O-deficient regions around the coatings surfaces. The third decoupling components observed at 532.14–532.96 eV (blue) is associated with the surface oxygen and/or OH-like species such as $Co(OH)_2$ phase/surface oxygen phase. The third components are also believed to be associated with the presence of weakly bonded O-species around the coatings surface to form H_2O and thereby absorbed species incorporated into the coating materials [67]. No significant changes in the surface bonding states of the CoZn-oxide thin film coatings were realized due to the variations in annealing temperatures and sol concentrations.

3.3 Nanoindentation analysis and FEM modeling: mechanical properties

3.3.1 Nanoindentation results

Ideally, for a rough surface the indentation depth should be much larger than the size of its surface features in order to obtain accurate results [68, 69]. However, in the case of the films being investigated, this is not practical as a higher depth will result in the substrate effect being involved. As such, three measures were conducted to facilitate measurement accuracy. Firstly, an indentation tip with a radius of ~700 nm was used, so that it could cover a large area to average out the roughness effect. Secondly, more data points were taken, typically > 100, and the mean values were adopted as more reliable experimental data. Thirdly, we used finite element modeling to estimate the influence of roughness on the results. Similar to the results in previous reports [70], the estimated roughness influence is approximately (10±3)% under estimation. The final experimental Young's modulus *E*, was derived from the indentation results and are shown in Figure 7, while the results were compared with that results from FEM modeling (see below). The elastic modulus *E* varied within the range of 43.7 GPa (S5) – 69.2 GPa (S7), which is

comparable with that in CoCuO films [71]. Due to the fact that the indentation is shallow (~ 0.2 mN), the hardness results based on the indention were deduced to be unreliable thus they are not presented here. By comparing the *E* data with the composition data, which is overlaid in Figure 7 with the scale shown on the right hand side, one may observe that there is a correlation between the two data sets – films with higher O concentration tend to have a higher Young's modulus.

3.3.2 FEM modeling

Based on the mechanical properties given by nanoindentation experiments, for FEM modeling investigation, the parameters of the substrate and indenter were proposed and are summarised in Table 4 [56, 72]. The load carrying capability of the films is frequently assessed by the equivalent stress, or von Mises stress, labelled as σ_{equiv}. This is a measure of the potential damage the level of stress could induce, and can be expressed by,

$$\sigma_{equiv} = \left\{0.5\left[\left(\sigma_{xx} - \sigma_{yy}\right)^2 + \left(\sigma_{yy} - \sigma_{zz}\right)^2 + \left(\sigma_{zz} - \sigma_{xx}\right)^2 + \left(\sigma_{xy} + \sigma_{yz} + \sigma_{zx}\right)^2\right]\right\}^{1/2} \qquad (3)$$

where σ_{xx}, σ_{yy}, σ_{zz}, σ_{xy}, σ_{yz}, σ_{zx} are the corresponding stress tensor components, respectively.

To compare the stress and strain levels in different films under the same loading using FEM, we set the loading at the top of the indenter to a constant force of 20 mN for different films, which was calculated through integration of the z component of the surface traction at the top surface of the indenter. The resulted indentation depths are shown in Figure 8 for the 4 samples (S5, S1, S3, and S7), the Young's modulus which spreads almost evenly across the complete range of the experimental *E* value defined by all the 9 samples under study. For the same loading condition, the indentation depth is inversely related to the Young's modulus of each film (Figure 8(b)). The depth for S5, which has the lowest modulus, is 20% less than that for S7. The FEM modelling results of stress distribution is given in Figure 9 for the 4 films. All the films are of 1.2 μm thickness and set on a silicon substrate. As expected, for films with a smaller Young's modulus (S5, S1) the maximum induced von Mises stress is lower, at about ~4 GPa. It is much higher in films having a greater modulus (S3, S7), about ~6 GPa. For all the films being studied, the maximum stress level is in the range of 4 – 6.5 GPa. Two types of substrate, Aluminium and silica, have been used in the modeling. There is no discernible difference between the results, which is possibly due to the fact that, both of the substrate materials have similar Young's modulus, which is higher than that of the films, and that both have a sufficiently high yield

strength so that no yield occurs in our modeling loading range. However, under the same loading, the film deformation, and correspondingly, the strain levels in the films, is much higher for those films with lower Young's modulus. This can be clearly seen through a comparison between the geometrical shapes in Figure 9. A higher level of strain will result in early yielding for films with smaller modulus.

In Figure 10, the stress distribution under different loadings are compared. For different loading levels, the higher the indentation depth, the higher the induced stress. The stress level at the top and bottom of the film is maintained at a relatively smaller value with respect to that at the center location, for all different loading levels. This is due to the difference between the Young's modulus of the film, the substrate and the indenter, with the latter two having higher moduli. Within the substrate, for lower loadings only a small stress level can be observed close to the interface. However with the increase of the indentation depth a significant stress level is observed which is almost comparable with the stress level in the film (Figure 11).

The influence of the film's thickness on the stress level and distributions are shown in Figures 12 and 13. Within the coating the stress maximum is located at about the midway point between the film surface and the film-substrate interface. Also due to the difference between the Young's modulus of the film and that of the substrate, a significant stress level is also observed in the substrate. When the thickness of the films increased from 1.0 μm to 1.6 μm, the maximum stress level in the film only reduced slightly. Meanwhile, the stress level at the surface and interface decreased more significantly, and a ~30% decrease of the stress within the substrate was observed.

3.4 Water contact angle measurements

The experimental results of water contact angles for all the samples are shown in Figure 14. The measured range was 96.4 -110.8°, which is thought to be moderately hydrophobic. The highest contact angles were observed in S4 (110.8°) and S7 (110.4°). The water contact angle is an important parameter for the materials used in energy applications such as solar film. To our best knowledge current the data for CoZn-oxide film are not available. So here we make a comparison between the contact angles of the CoZn-oxide with that of other solar film materials. For example, for Al_2O_3 materials, the reported contact angle is between 120° ~ 163° [73, 74].

It has been well established that the contact angle between a liquid and smooth solid surface in air is described by Young's equation [75] $\cos\gamma = (\gamma_{sv} - \gamma_{sl})/\gamma_{sv}$, where γ refers to the interfacial tension and the subscripts s, l, and v refer to the solid, liquid, and vapor phases, respectively. The interfacial tensions are determined by the chemical compositions of the solid and liquid phases. However, on a rough solid surface, the contact angle will be different from that on a smooth surface of the same composition. When the experimental contact angle results are plotted together with the surface roughness, it is found that there exists a good correlation between these two sets of data (Figure 15), which suggests that for the samples being studied, surface roughness plays a more important role in deciding the variation of the contact angle, while the change in composition has less of an effect. Wenzel [76] and Cassie and Baxter [77] proposed two most frequently used models to estimate the effect of roughness on the apparent contact angle of liquid drops. The Wenzel model recognizes that surface roughness increases the available surface area of the solid, which modifies the surface contact angle according to the expression, $\cos\theta^* = r\cos\theta$, where θ^* is the apparent contact angle on the textured surface, r is the surface roughness factor, and θ is the equilibrium contact angle on a smooth surface of the same material, which can be derived from Young's equation. Our results qualitatively agree with this equation, the higher the roughness of the surface, the larger the contact angle will be.

Different techniques and evaluation methods have been proposed to evaluate the contact angle on different surface configurations [78] and modify the contact angle of the materials [79, 80] in order to improve and enhance their suitability and functionality in real applications. The determination of the "intrinsic" contact angle for the series of the films with different compositions is expected to be a good starting point for customized designs of the films towards variable applications.

4. Conclusions

A series of sol-gel spin-coated CoZn-oxide thin film coatings, synthesized with various sol concentrations and annealing temperatures were investigated using different experimental and modeling techniques. Atomic force microscopic analysis indicated a monotonic increase in the average and rms values for the surface roughness of these coatings with the rise in sol strength. The highest value of the average and rms values of the surface roughness of CoZn-oxide

coatings was recorded to be 84.4 and 109 nm, respectively. The atomic compositions of the deposited coatings confirmed via XPS survey scans show that the Co and Zn contents in the coating structures slightly increased at higher sol concentrations. High resolution XPS analysis was conducted to identify the local bonding states of these elements and formations of various cobalt oxides, cobalt hydroxides, zinc oxides, metal Co, Metal Zn, surface oxygen and/or OH-like species were detected. From the nanoindentation data the Young's moduli of the films were determined. A correlation exists between the O concentration and the mechanical property – films with higher O concentration tend to have higher Young's modulus. The elastic modulus *E* varied within the range of 43.7 GPa – 69.2 GPa, which is comparable with that in CoCuO films. Film S7 has the highest Young's modulus 69.2 GPa, which shows a 58% increase from that of S5, owing to the increase in the O concentration. The FEM modelling results indicate that, while under the same loading, the film deformation and strain levels in the films is higher for those films with lower Young's modulus, while the von-Mises stress is higher. Because of the large difference between the modulus of the film, and that of the substrate and the indenter, the stress concentration will be midway between the film surface and the interface. For the same reason large stress is also observed within the substrate when the film is thin, and when the indentation depth is large. A reasonable hydrophobicity of these surface was given the fact of the measured range of water contact angle to be 96.4 -110.8°. Higher roughness correlates with a higher contact angle, while the composition of the films seems to have little influence on the contact angle. Therefore, it is possible to achieve an optimized design of the water contact angle through adjustments of the surface roughness of the films.

Acknowledgements

This research work was financially supported by IRU-MRUN Collaborative Research Program (2015-2018, Australia). Amun Amri gratefully acknowledges the financial support of the Indonesian Government. M Mahbubur Rahman gratefully acknowledges the support of Jahangirnagar University.

References

[1] Q. Zhang, K. Zhang, D. Xu, G. Yang, H. Huang, F. Nie, C. Liu, S. Yang, CuO nanostructures: Synthesis, characterization, growth mechanisms, fundamental properties, and applications, Progress in Materials Science, 60 (2014) 208-237.
[2] J. Safari, Z. Zarnegar, Advanced drug delivery systems: Nanotechnology of health design A review, Journal of Saudi Chemical Society, 18 (2014) 85-99.
[3] Z. Zhang, C. Shao, X. Li, C. Wang, M. Zhang, Y. Liu, Electrospun nanofibers of p-type NiO/n-type ZnO heterojunctions with enhanced photocatalytic activity, ACS Applied Materials and Interfaces, 2 (2010) 2915-2923.
[4] C.W. Na, H.S. Woo, I.D. Kim, J.H. Lee, Selective detection of NO_2 and C_2H_5OH using a Co_3O_4-decorated ZnO nanowire network sensor, Chemical Communications, 47 (2011) 5148-5150.
[5] M.A. Kanjwal, F.A. Sheikh, N.A.M. Barakat, I.S. Chronakis, H.Y. Kim, Co3O4-ZnO hierarchical nanostructures by electrospinning and hydrothermal methods, Applied Surface Science, 257 (2011) 7975-7981.
[6] J.H. Hsieh, P.W. Kuo, K.C. Peng, S.J. Liu, J.D. Hsueh, S.C. Chang, Opto-electronic properties of sputter-deposited Cu_2O films treated with rapid thermal annealing, Thin Solid Films, 516 (2008) 5449-5453.
[7] D. Bekermann, A. Gasparotto, D. Barreca, C. Maccato, E. Comini, C. Sada, G. Sberveglieri, A. Devi, R.A. Fischer, Co_3O_4/ZnO nanocomposites: From plasma synthesis to gas sensing applications, ACS Applied Materials and Interfaces, 4 (2012) 928-934.
[8] B. Shouli, C. Liangyuan, L. Dianqing, Y. Wensheng, Y. Pengcheng, L. Zhiyong, C. Aifan, C.C. Liu, Different morphologies of ZnO nanorods and their sensing property, Sensors and Actuators, B: Chemical, 146 (2010) 129-137.
[9] R. Saravanan, H. Shankar, G. Rajasudha, A. Stephen, V. Narayanan, Photocatalytic degradation of organic dye using nano ZnO, International Journal of Nanoscience, 10 (2011) 253-257.
[10] M. Giannouli, F. Spiliopoulou, Effects of the morphology of nanostructured ZnO films on the efficiency of dye-sensitized solar cells, Renewable Energy, 41 (2012) 115-122.
[11] J. Zhao, L. Wang, X. Yan, Y. Yang, Y. Lei, J. Zhou, Y. Huang, Y. Gu, Y. Zhang, Structure and photocatalytic activity of Ni-doped ZnO nanorods, Materials Research Bulletin, 46 (2011) 1207-1210.
[12] G. Liu, G. Li, X. Qiu, L. Li, Synthesis of ZnO/titanate nanocomposites with highly photocatalytic activity under visible light irradiation, Journal of Alloys and Compounds, 481 (2009) 492-497.
[13] S. Khanchandani, S. Kundu, A. Patra, A.K. Ganguli, Shell thickness dependent photocatalytic properties of ZnO/CdS core-shell nanorods, Journal of Physical Chemistry C, 116 (2012) 23653-23662.
[14] W.Y. Li, L.N. Xu, J. Chen, Co3O4 nanomaterials in lithium-ion batteries and gas sensors, Advanced Functional Materials, 15 (2005) 851-857.

[15] S. Elhag, Z.H. Ibupoto, O. Nour, M. Willander, Synthesis of Co3O4 cotton-like nanostructures for cholesterol biosensor, Materials, 8 (2015) 149-161.
[16] X.H. Xia, J.P. Tu, Y.J. Mai, X.L. Wang, C.D. Gu, X.B. Zhao, Self-supported hydrothermal synthesized hollow Co3O4 nanowire arrays with high supercapacitor capacitance, Journal of Materials Chemistry, 21 (2011) 9319-9325.
[17] S.A. Makhlouf, Z.H. Bakr, K.I. Aly, M.S. Moustafa, Structural, electrical and optical properties of Co3O 4 nanoparticles, Superlattices and Microstructures, 64 (2013) 107-117.
[18] M. Grzelczak, J. Zhang, J. Pfrommer, J. Hartmann, M. Driess, M. Antonietti, X. Wang, Electro- and photochemical water oxidation on ligand-free Co 3O4 nanoparticles with tunable sizes, ACS Catalysis, 3 (2013) 383-388.
[19] X. Wang, L. Yu, X.L. Wu, F. Yuan, Y.G. Guo, Y. Ma, J. Yao, Synthesis of single-crystalline Co3O4 octahedral cages with tunable surface aperture and their lithium storage properties, Journal of Physical Chemistry C, 113 (2009) 15553-15558.
[20] A. Matsuda, R. Yamauchi, D. Shiojiri, G. Tan, S. Kaneko, M. Yoshimoto, Room-temperature selective epitaxial growth of CoO (1 1 1) and Co<inf>3</inf>O<inf>4</inf> (1 1 1) thin films with atomic steps by pulsed laser deposition, Applied Surface Science, 349 (2015) 78-82.
[21] H. Xu, Q. Zhao, H. Yang, Y. Chen, Study of magnetic properties of ZnO nanoparticles codoped with Co and Cu, Journal of Nanoparticle Research, 11 (2009) 615-621.
[22] T.T. Loan, N.N. Long, L.H. Ha, Photoluminescence properties of Co-doped ZnO nanorods synthesized by hydrothermal method, Journal of Physics D: Applied Physics, 42 (2009).
[23] O.D. Jayakumar, C. Sudakar, C. Persson, H.G. Salunke, R. Naik, A.K. Tyagi, Enhancement of ferromagnetic properties in Zn0.95 Co 0.05O nanoparticles by indium codoping: An experimental and theoretical study, Applied Physics Letters, 97 (2010).
[24] R.N. Aljawfi, S. Mollah, Properties of Co/Ni codoped ZnO based nanocrystalline DMS, Journal of Magnetism and Magnetic Materials, 323 (2011) 3126-3132.
[25] S.S. Abdullahi, Y. Köseoğlu, S. Güner, S. Kazan, B. Kocaman, C.E. Ndikilar, Synthesis and characterization of Mn and Co codoped ZnO nanoparticles, Superlattices and Microstructures, 83 (2015) 342-352.
[26] M. Yang, Z. Guo, K. Qiu, J. Long, G. Yin, D. Guan, S. Liu, S. Zhou, Synthesis and characterization of Mn-doped ZnO column arrays, Applied Surface Science, 256 (2010) 4201-4205.
[27] H. Yang, S. Nie, Preparation and characterization of Co-doped ZnO nanomaterials, Materials Chemistry and Physics, 114 (2009) 279-282.
[28] G. Mohan Kumar, P. Ilanchezhiyan, J. Kawakita, M. Subramanian, R. Jayavel, Magnetic and optical property studies on controlled low-temperature fabricated one-dimensional Cr doped ZnO nanorods, CrystEngComm, 12 (2010) 1887-1892.
[29] Z.N. Kayani, R. Ishaque, B. Zulfiqar, S. Riaz, S. Naseem, Fabrication and characterization of nanocrystalline Al, Co:ZnO thin films by a sol–gel dip coating, Optical and Quantum Electronics, 49 (2017) 223.

[30] Y. Köseoğlu, Fuel aided rapid synthesis and room temperature ferromagnetism of M0.1Co0.1Zn0.8O (M=Mn, Ni, Fe and Cu) DMS nanoparticles, Ceramics International, 42 (2016) 9190-9195.
[31] T.K. Jana, A. Pal, K. Chatterjee, Magnetic and photocatalytic study of Co3O4–ZnO nanocomposite, Journal of Alloys and Compounds, 653 (2015) 338-344.
[32] S.A. El-Molla, L.I. Ali, H.R. Mahmoud, M.M. Ibrahim, M.A. Naghmash, Effect of preparation method, loading of Co3O4 and calcination temperature on the physicochemical and catalytic properties of Co3O4/ZnO nanomaterials, Materials Chemistry and Physics, 185 (2017) 44-54.
[33] Christian Brosseaua, Stéphane Mallégol, P. Quéffélec, Electromagnetism and magnetization in granular two-phase nanocomposites: A comparative microwave study, Journal of Applied Physics, 101 (2007) 034301.
[34] M. Arucu, Diluted magnetic semiconductor: Structure, size and shape, and magnetic properties, Turkish Journal of Physics, 41 (2017) 20-24.
[35] L.E. Brus, Electron-electron and electron-hole interactions in small semiconductor crystallites: The size dependence of the lowest excited electronic state, The Journal of Chemical Physics, 80 (1984) 4403-4409.
[36] A.P. Alivisatos, Perspectives on the physical chemistry of semiconductor nanocrystals, Journal of Physical Chemistry, 100 (1996) 13226-13239.
[37] M.A. Ibragimova, A.L. Kozlovskiy, I.E. Kenzhina, M.V. Zdorovets, Influence of the applied potentials difference on structural and conductive properties of CoZnO nanotubes, Materials Research Express, 5 (2018) 045010.
[38] Z.N. Kayani, A. Afzal, E.S. Khan, F. Nazir, F. Saleemi, S. Riaz, S. Naseem, Structural and Magnetic Properties of CoZnO Films, Materials Today: Proceedings, 2 (2015) 5473-5476.
[39] S. Roguai, A. Djelloul, C. Nouveau, T. Souier, A.A. Dakhel, M. Bououdina, Structure, microstructure and determination of optical constants from transmittance data of co-doped Zn0.90Co0.05M0.05O (MAl, Cu, Cd, Na) films, Journal of Alloys and Compounds, 599 (2014) 150-158.
[40] M. Soylu, B. Coskun, A.G. Al-Sehemi, A.A. Al-Ghamdi, F. Yakuphanoglu, The validity of Kohlrausch law for the photocurrent transient and the role of N2/Ar flow ratio in photoconductivity of sputtered CoZnO, Journal of Alloys and Compounds, 712 (2017) 152-163.
[41] R.K. Sharma, R. Ghose, Synthesis of Co3O4–ZnO mixed metal oxide nanoparticles by homogeneous precipitation method, Journal of Alloys and Compounds, 686 (2016) 64-73.
[42] X. Zhao, F. Zhang, S. Xu, D.G. Evans, X. Duan, From layered double hydroxides to ZnO-based mixed metal oxides by thermal decomposition: Transformation mechanism and UV-blocking properties of the product, Chemistry of Materials, 22 (2010) 3933-3942.
[43] M. Pang, G. Long, S. Jiang, Y. Ji, W. Han, B. Wang, X. Liu, Y. Xi, D. Wang, F. Xu, Ethanol-assisted solvothermal synthesis of porous nanostructured cobalt oxides (CoO/Co<inf>3</inf>O<inf>4</inf>) for high-performance supercapacitors, Chemical Engineering Journal, 280 (2015) 377-384.

[44] L. Gu, L. Qian, Y. Lei, Y. Wang, J. Li, H. Yuan, D. Xiao, Microwave-assisted synthesis of nanosphere-like NiCo2O 4 consisting of porous nanosheets and its application in electro-catalytic oxidation of methanol, Journal of Power Sources, 261 (2014) 317-323.
[45] E. Amini, M. Rezaei, Preparation of mesoporous Fe-Cu mixed metal oxide nanopowder as active and stable catalyst for low-temperature CO oxidation, Cuihua Xuebao/Chinese Journal of Catalysis, 36 (2015) 1711-1718.
[46] N. Salah, S.S. Habib, Z.H. Khan, A. Memic, A. Azam, E. Alarfaj, N. Zahed, S. Al-Hamedi, High-energy ball milling technique for ZnO nanoparticles as antibacterial material, International journal of nanomedicine, 6 (2011) 863-869.
[47] M. Saif, H. Hafez, A.I. Nabeel, Photo-induced self-cleaning and sterilizing activity of Sm3+ doped ZnO nanomaterials, Chemosphere, 90 (2013) 840-847.
[48] A.J. Kulandaisamy, C. Karthek, P. Shankar, G.K. Mani, J.B.B. Rayappan, Tuning selectivity through cobalt doping in spray pyrolysis deposited ZnO thin films, Ceramics International, 42 (2016) 1408-1415.
[49] M.L. Dinesha, H.S. Jayanna, S. Mohanty, S. Ravi, Structural, electrical and magnetic properties of Co and Fe co-doped ZnO nanoparticles prepared by solution combustion method, Journal of Alloys and Compounds, 490 (2010) 618-623.
[50] H.A. Miran, M.M. Rahman, Z.-T. Jiang, M. Altarawneh, L.S. Chuah, H.-L. Lee, E. Mohammedpur, A. Amri, N. Mondinos, B.Z. Dlugogorski, Structural and optical characteristics of pre- and post-annealed sol-gel derived CoCu-oxide coatings, Journal of Alloys and Compounds, 701 (2017) 222-235.
[51] A.A. Taysioglu, A. Peksoz, Y. Kaya, N. Derebasi, G. Irez, G. Kaynak, GMI effect in CuO coated Co-based amorphous ribbons, Journal of Alloys and Compounds, 487 (2009) 38-41.
[52] J.G. Swadener, G.M. Pharr, A methodology for the calibration of spherical indenters, MRS Online Proceedings Library Archive, 594 (1999).
[53] Z. Li, P. Munroe, Z.-t. Jiang, X. Zhao, J. Xu, Z.-f. Zhou, J.-q. Jiang, F. Fang, Z.-h. Xie, Designing superhard, self-toughening CrAlN coatings through grain boundary engineering, Acta Materialia, 60 (2012) 5735-5744.
[54] Khalil Ibrahim, M Mahbubur Rahman, Xiaoli Zhao, Jean-Pierre Veder, Zhi-feng Zhou, Ehsan Mohammadpour, Ridha Hameed Majeed, Aleksandar N Nikoloski, Z.-T. Jiang, Annealing effects on microstructural, optical, and mechanical properties of sputtered CrN thin film coatings: Experimental studies and finite element modeling, Journal of Alloys and Compounds, 750 (2018) 451-464.
[55] E.J. Dickinson, H. Ekström, E. Fontes, COMSOL Multiphysics®: Finite element software for electrochemical analysis. A mini-review, Electrochemistry communications, 40 (2014) 71-74.
[56] A. Amri, Z.T. Jiang, X. Zhao, Z. Xie, C.Y. Yin, N. Ali, N. Mondinos, M.M. Rahman, D. Habibi, Tailoring the physicochemical and mechanical properties of optical copper-cobalt oxide thin films through annealing treatment, Surface and Coatings Technology, 239 (2014) 212-221.

[57] P.C. Wo, X.L. Zhao, P.R. Munroe, Z.F. Zhou, K.Y. Li, D. Habibi, Z.H. Xie, Extremely hard, damage-tolerant ceramic coatings with functionally graded, periodically varying architecture, Acta Materialia, 61 (2013) 193-204.
[58] X. Zhao, Z. Xie, P. Munroe, Nanoindentation of hard multilayer coatings: Finite element modelling, Materials Science and Engineering A, 528 (2011) 1111-1116.
[59] R. Dey, R. Bhunia, S. Hussain, B.R. Chakraborty, R. Bhar, A.K. Pal, Flexible and free-standing films containing cobalt-doped nanocrystalline zinc oxide dispersed in polyvinylidene fluoride matrix: synthesis and characterization, Polymer Bulletin, 75 (2018) 307-325.
[60] A. Amri, Z.T. Jiang, P.A. Bahri, C.Y. Yin, X. Zhao, Z. Xie, X. Duan, H. Widjaja, M.M. Rahman, T. Pryor, Surface electronic structure and mechanical characteristics of copper-cobalt oxide thin film coatings: Soft X-ray synchrotron radiation spectroscopic analyses and modeling, Journal of Physical Chemistry C, 117 (2013) 16457-16467.
[61] J.T. S., K.J. H., B.S. J., Y.C. J., Depth-profile analysis from X-ray photoelectron spectroscopy on As-implanted ZnO activated in ozone ambient, Crystal Research and Technology, 43 (2008) 289-292.
[62] A.S. Kamble, R.C. Pawar, N.L. Tarwal, L.D. More, P.S. Patil, Ethanol sensing properties of chemosynthesized CdO nanowires and nanowalls, Materials Letters, 65 (2011) 1488-1491.
[63] N.L. Tarwal, A.V. Rajgure, A.I. Inamdar, R.S. Devan, I.Y. Kim, S.S. Suryavanshi, Y.R. Ma, J.H. Kim, P.S. Patil, Growth of multifunctional ZnO thin films by spray pyrolysis technique, Sens Actuators A Phys, 199 (2013) 67-73.
[64] J.L. Gautier, E. Trollund, E. Ríos, P. Nkeng, G. Poillerat, Characterization of thin CuCo2O4 films prepared by chemical spray pyrolysis. Study of their electrochemical stability by ex situ spectroscopic analysis, Journal of Electroanalytical Chemistry, 428 (1997) 47-56.
[65] G. Tyuliev, D. Panayotov, I. Avramova, D. Stoichev, T. Marinova, Thin-film coating of Cu-Co oxide catalyst on lanthana/zirconia films electrodeposited on stainless steel, Materials Science and Engineering C, 23 (2003) 117-121.
[66] A. La Rosa-Toro, R. Berenguer, C. Quijada, F. Montilla, E. Morallón, J.L. Vázquez, Preparation and Characterization of Copper-Doped Cobalt Oxide Electrodes, The Journal of Physical Chemistry B, 110 (2006) 24021-24029.
[67] T.C. Li, C.F. Han, T.H. Kuan, J.F. Lin, Effects of sputtering-deposition inclination angle on the IGZO film microstructures, optical properties and photoluminescence, Opt. Mater. Express, 6 (2016) 343-366.
[68] S. Chung, A. Yap, Effects of surface finish on indentation modulus and hardness of dental composite restoratives, Dental Materials, 21 (2005) 1008-1016.
[69] W.-G. Jiang, J.-J. Su, X.-Q. Feng, Effect of surface roughness on nanoindentation test of thin films, Engineering Fracture Mechanics, 75 (2008) 4965-4972.
[70] C. Walter, T. Antretter, R. Daniel, C. Mitterer, Finite element simulation of the effect of surface roughness on nanoindentation of thin films with spherical indenters, Surface and coatings technology, 202 (2007) 1103-1107.

[71] A. Amri, Z.-T. Jiang, P.A. Bahri, C.-Y. Yin, X. Zhao, Z. Xie, X. Duan, H. Widjaja, M.M. Rahman, T. Pryor, Surface electronic structure and mechanical characteristics of copper–cobalt oxide thin film coatings: soft x-ray synchrotron radiation spectroscopic analyses and modeling, The Journal of Physical Chemistry C, 117 (2013) 16457-16467.
[72] X. Zhao, Z. Xie, P. Munroe, Nanoindentation of hard multilayer coatings: Finite element modelling, Materials Science and Engineering: A, 528 (2011) 1111-1116.
[73] K. Tadanaga, N. Katata, T. Minami, Super□water□repellent Al2O3 coating films with high transparency, Journal of the American ceramic society, 80 (1997) 1040-1042.
[74] K. Tadanaga, N. Katata, T. Minami, Formation Process of Super□Water□Repellent Al2O3 Coating Films with High Transparency by the Sol–Gel Method, Journal of the American Ceramic Society, 80 (1997) 3213-3216.
[75] T. Young, III. An essay on the cohesion of fluids, Philosophical transactions of the royal society of London, 95 (1805) 65-87.
[76] R.N. Wenzel, Resistance of solid surfaces to wetting by water, Industrial & Engineering Chemistry, 28 (1936) 988-994.
[77] A. Cassie, S. Baxter, Wettability of porous surfaces, Transactions of the Faraday society, 40 (1944) 546-551.
[78] A. Dupuis, J. Yeomans, Modeling droplets on superhydrophobic surfaces: equilibrium states and transitions, Langmuir, 21 (2005) 2624-2629.
[79] C.M. Bollenl, P. Lambrechts, M. Quirynen, Comparison of surface roughness of oral hard materials to the threshold surface roughness for bacterial plaque retention: a review of the literature, Dental materials, 13 (1997) 258-269.
[80] E. Bittoun, A. Marmur, The role of multiscale roughness in the lotus effect: is it essential for super-hydrophobicity?, Langmuir, 28 (2012) 13933-13942.

Table 1. Surface roughness parameters of sol-gel derived CoZnO thin film coatings estimated *via* AFM studies.

Sample	Mean roughness, R_a (nm)	rms value of surface roughness, R_q (nm)	Maximum surface roughness, R_m (nm)	*z* Scale (nm)	Image surface area (μm^2)
S1	35.4	43.9	286	286	27.6
S2	26.8	33.5	242	240	106
S3	22.5	29.2	296	296	105
S4	56.5	69.8	449	450	32.4
S5	30.3	38.0	354	354	108
S6	16.8	20.8	160	170	25.5
S7	84.4	105	659	1100	62.6
S8	43.1	55.6	382	386	27.5
S9	10.9	13.6	755	749	33.6

Table 2. Atomic compositions of sol-gel derived CoZnO thin film coatings as estimated *via* XPS measurements.

Samples	Elements	Atomic percentages of elements (%)
S1	Co	14.40
	Zn	10.95
	O	74.65
S2	Co	15.0
	Zn	11.70
	O	73.30
S3	Co	16.0
	Zn	12.68
	O	71.32
S4	Co	16.19
	Zn	12.72
	O	71.19
S5	Co	18.90
	Zn	13.20
	O	67.90
S6	Co	19.68
	Zn	15.45
	O	65.87
S7	Co	10.74
	Zn	8.09
	O	81.17
S8	Co	11.15
	Zn	12.24
	O	76.62
S9	Co	12.08
	Zn	11.74
	O	76.18

Table 3. XPS fitting results of sol-gel derived CoZnO thin film coatings for the core level binding energies.

Samples	Photoelectron lines	Bonding states	BE (eV)	FWHM (eV)	Percentages of the component (%)
S1	Co2*p3/2*	Co_3O_4/CoO/Co_2O_3 phase	780.5	2.9	50.6
		Co_2O_3/ $Co(OH)_2$ phase	782.6	2.9	26.3
	Co2*p3/2* sat.	Co_2O_3 phase	786.6	3.8	23.1
	O1*s*	Co_3O_4/CoO/ZnO phase	530.3	1.3	52.3
		Co_3O_4/ZnO/$Co(OH)_2$ phase	531.2	1.2	18.1
		$Co(OH)_2$ phase/Surface oxygen	532.3	1.6	29.6
	Zn2*p3/2*	Metal Zn/ZnO	1021.7	1.4	42.8
		ZnO phase	1022.5	1.4	25.3
S2	Co2*p3/2*	Co_3O_4/CoO/Co_2O_3 phase	780.2	1.5	43.9
		Co_2O_3/ $Co(OH)_2$ phase	782.6	3.0	43.4
	Co2*p3/2* sat.	Co_2O_3 phase	786.3	3.0	12.7
	O1*s*	Co_3O_4/CoO/ZnO phase	530.4	1.5	49.0
		ZnO/$Co(OH)_2$ phase	531.8	1.5	33.9
		Surface oxygen	533.0	1.5	17.1
	Zn2*p3/2*	Metal Zn/ZnO	1021.6	1.3	38.5
		ZnO phase	1022.4	1.3	28.4
S3	Co2*p3/2*	Metal Co/Co_3O_4 phase	779.1	2.72	17.9
		CoO/ Co_2O_3/Co_3O_4/$Co(OH)_2$ phase	781.4	3.9	60.5
	Co2*p3/2* sat.	Co_2O_3 phase	786.7	3.9	21.6
	O1*s*	Co_3O_4/CoO/ZnO phase	530.3	1.33	44.4
		Co_3O_4/ZnO/$Co(OH)_2$ phase	530.9	1.62	28.1
		$Co(OH)_2$ phase/Surface oxygen	532.3	1.90	27.5
	Zn2*p3/2*	Metal Zn/ZnO	1021.52	1.23	26.8
		ZnO phase	1022.36	1.30	38.9
S4	Co2*p3/2*	Co_3O_4/CoO/Co_2O_3 phase	780.72	3.09	53.1
		$Co(OH)_2$ phase	783.21	3.7	24.8
	Co2*p3/2* sat.	Co_3O_4/Co_2O_3 phase	787.21	3.5	22.1
	O1*s*	Co_3O_4/CoO/ZnO phase	530.14	1.28	35.8
		Co_3O_4/ZnO/$Co(OH)_2$ phase	530.79	1.38	29.2
		$Co(OH)_2$ phase/Surface oxygen	532.06	1.90	35.0
	Zn2*p3/2*	Metal Zn/ZnO	1021.54	1.3	35.4
		ZnO phase	1022.37	1.3	32.0
S5	Co2*p3/2*	Co_2O_3/CoO/Co_3O_4/$Co(OH)_2$ phase	781.09	0.99	20.9
		$Co(OH)_2$ phase	782.59	3.30	58.3
	Co2*p3/2* sat.	Co_2O_3 phase	786.47	2.90	20.8
	O1*s*	Co_3O_4/ZnO/$Co(OH)_2$ phase	530.83	1.23	36.0
		ZnO/$Co(OH)_2$ phase	531.54	1.37	20.0
		Surface oxygen	532.86	2.30	44.0
	Zn2*p3/2*	Metal Zn/ZnO	1022.6	1.29	29.3

		ZnO phase	1023.1	1.30	36.8
S6	Co2*p3/2*	Co_3O_4 phase	778.5	0.98	20.3
		Co_2O_3 phase	780.4	3.9	63.2
	Co2*p3/2* sat.	Co_3O_4/Co_2O_3 phase	785.6	4.5	16.5
	O1*s*	Co_3O_4/CoO/ZnO phase	530.2	1.30	37.7
		Co_3O_4/ZnO phase	530.7	1.46	27.2
		$Co(OH)_2$ phase/Surface oxygen	532.1	2.00	35.1
	Zn2*p3/2*	Metal Zn/ZnO	1021.8	1.50	47.2
		ZnO phase	1022.4	1.44	21.0
S7	Co2*p3/2*	Metal Co/ Co_2O_3/CoO/Co_3O_4/$Co(OH)_2$ phase	780.1	2.85	38.0
		$Co(OH)_2$ phase	782.3	3.0	30.2
	Co2*p3/2* sat.	Co_2O_3 phase	786.5	4.9	31.8
	O1*s*	Co_3O_4/CoO/ZnO phase	529.8	1.57	24.8
		ZnO/$Co(OH)_2$ phase	531.6	2.00	42.0
		Surface oxygen	532.7	2.00	33.2
	Zn2*p3/2*	Metal Zn/ZnO	1021.5	1.99	46.8
		ZnO phase	1023.1	2.04	20.2
S8	Co2*p3/2*	Co_3O_4 phase	779.1	1.73	19.6
		$Co(OH)_2/Co_2O_3$ phase	781.4	3.0	53.8
	Co2*p3/2* sat.	Co_2O_3 phase	786.0	4.9	26.6
	O1*s*	Co_3O_4/ZnO phase	530.7	1.42	41.0
		$Co(OH)_2$ phase	532.1	1.80	32.7
		Surface oxygen	532.9	1.80	26.3
	Zn2*p3/2*	Metal Zn/ZnO	1022.1	1.5	46.9
		ZnO phase	1022.9	1.4	22.0
S9	Co2*p3/2*	Metal Co	778.6	1.84	21.2
		Co_2O_3/CoO/Co_3O_4/$Co(OH)_2$ phase	781.0	3.85	53.3
	Co2*p3/2* sat.	Co_2O_3 phase	786.0	3.50	19.5
	O1*s*	Co_3O_4/CoO/ZnO phase	530.1	1.43	40.6
		Co_3O_4/ZnO/$Co(OH)_2$ phase	531.4	2.00	30.6
		$Co(OH)_2$ phase/Surface oxygen	532.6	2.00	28.8
	Zn2*p3/2*	Metal Zn/ZnO	1021.5	1.20	37.9
		ZnO phase	1022.5	1.20	29.4

Table 4. FEM Modeling parameters of substrate and the diamond indenter.

Samples name	Young's modulus, E (GPa)	Poisson's ratio	Yield strength (MPa)
Aluminium	69	0.3	95
Silica	66.3	0.25	50
Indenter (DM)	1141	0.07	-

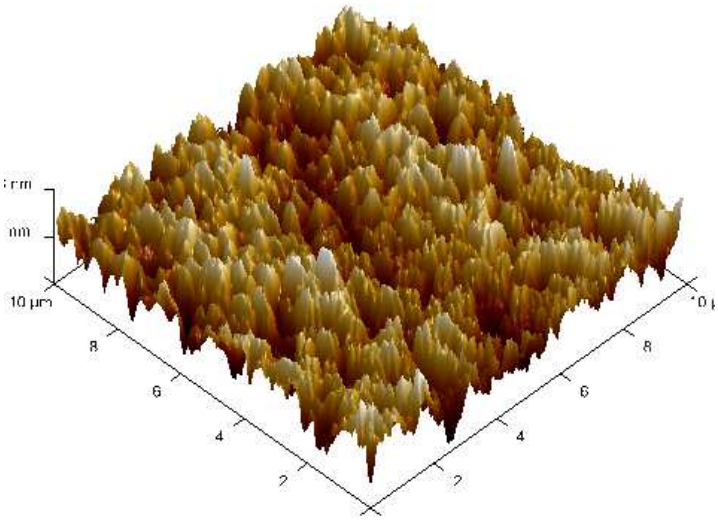

S-1

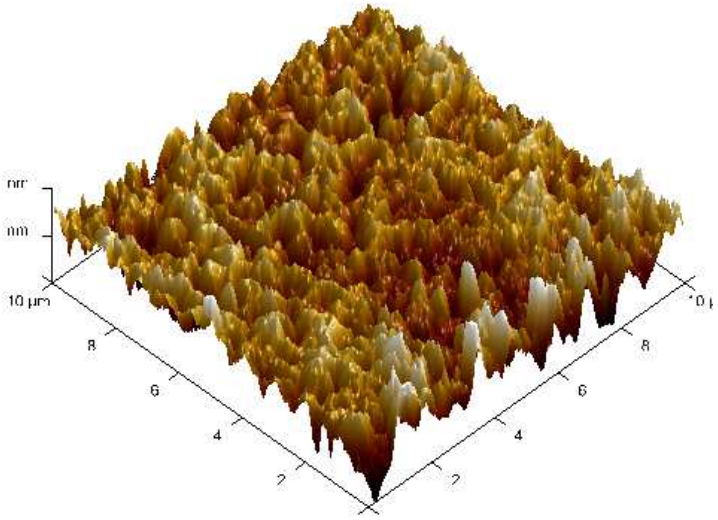

S-2

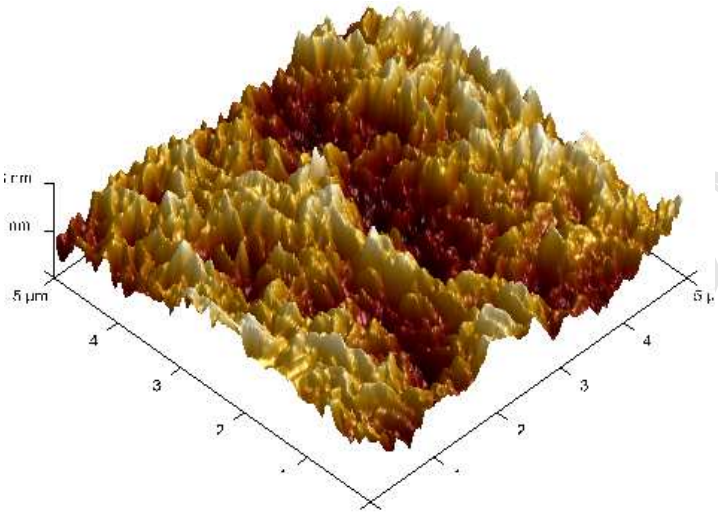

S-3

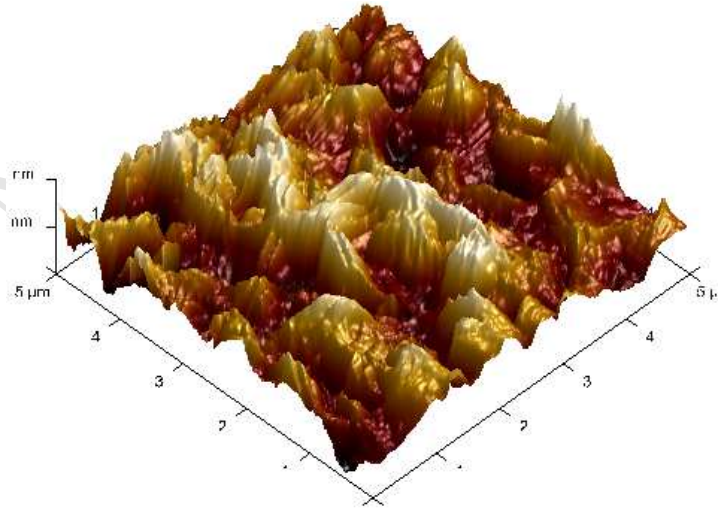

S-4

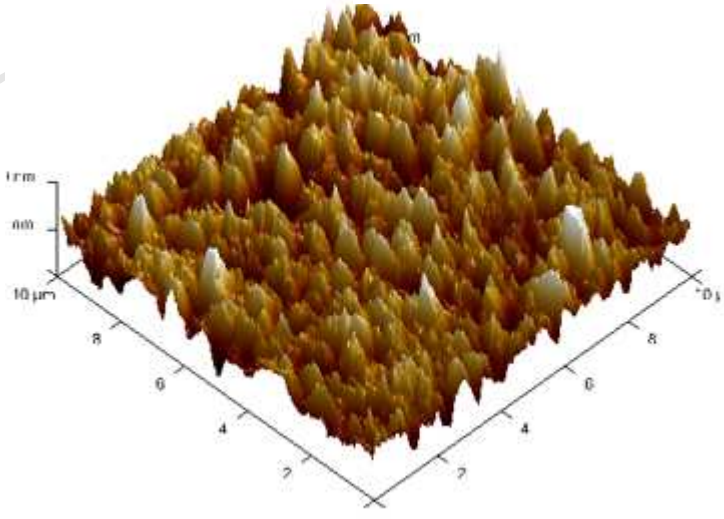

S-5

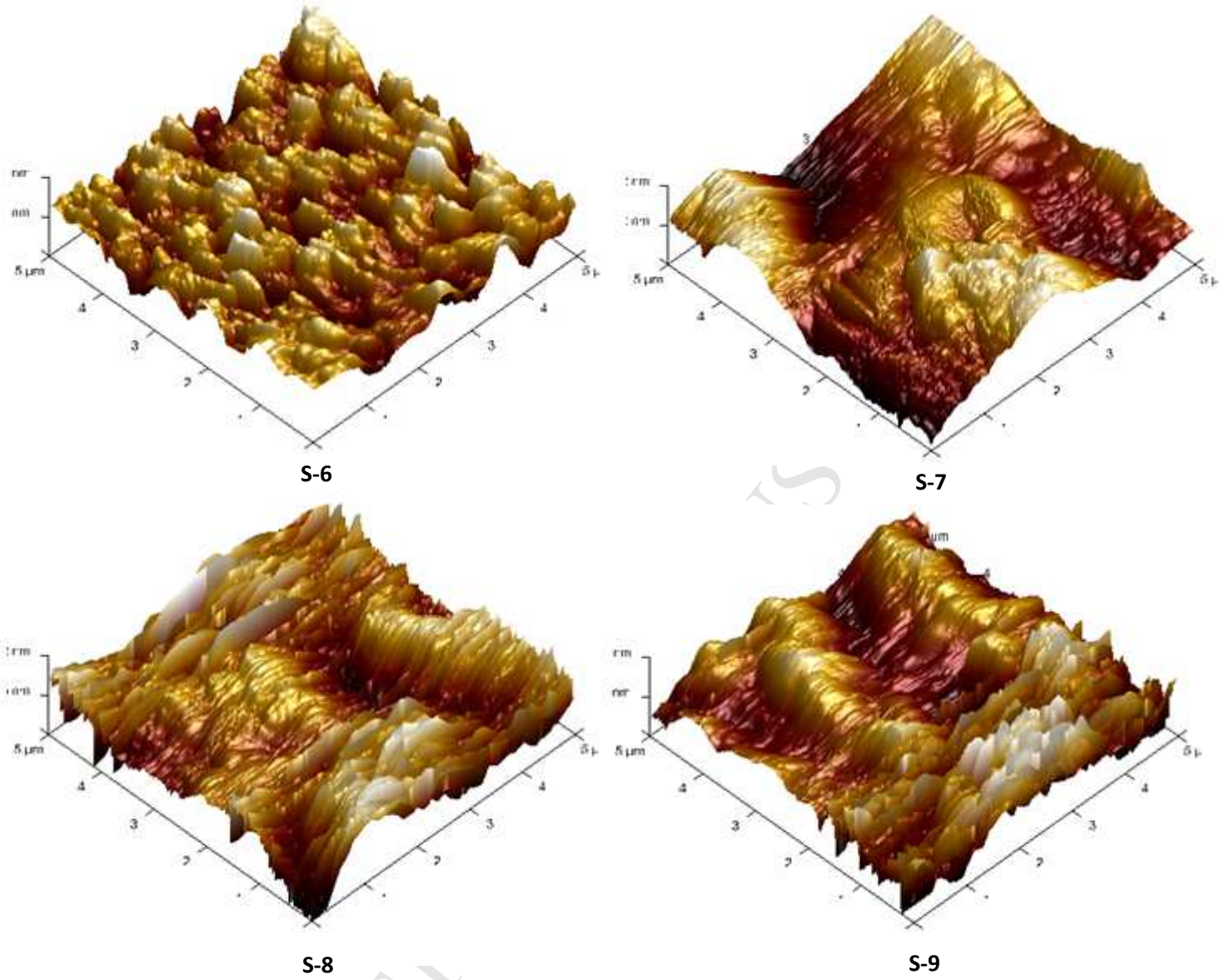

Figure1. AFM images of sol-gel derived CoZnO thin film coatings.

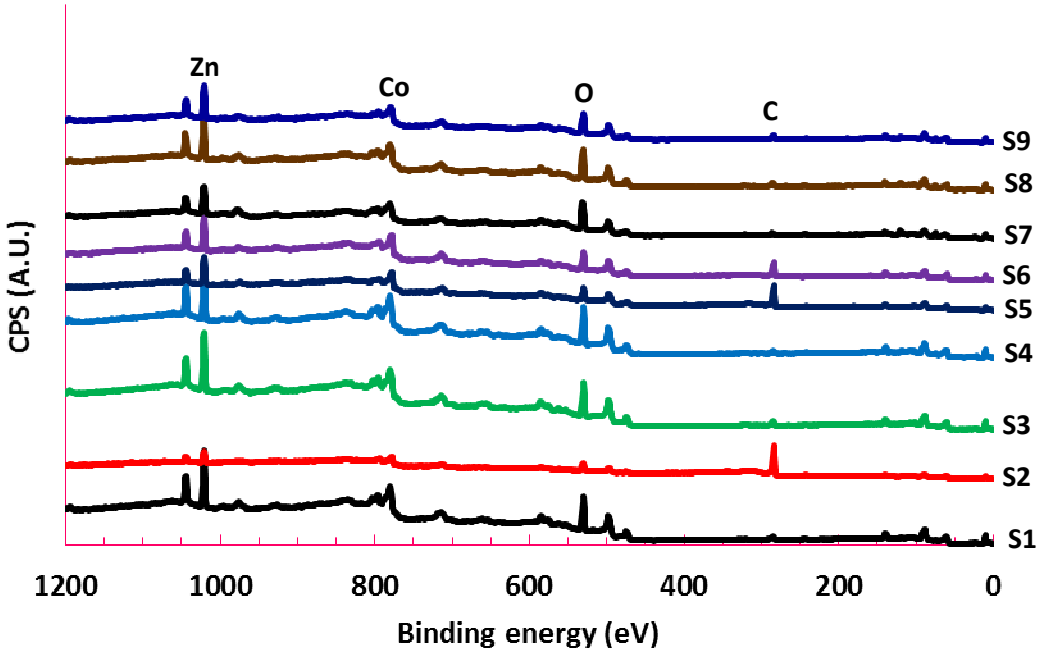

Figure 2. XPS survey scans of sol-gel derived CoZnO thin film coatings.

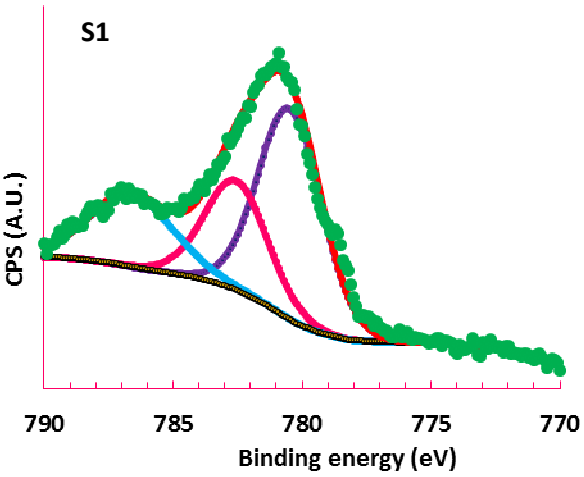
S1
CPS (A.U.)
790
785
780
775
770
Binding energy (eV)

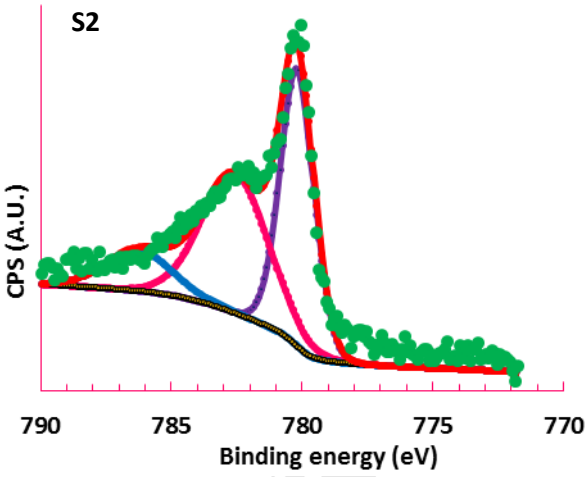
S2
CPS (A.U.)
790
785
780
775
770
Binding energy (eV)

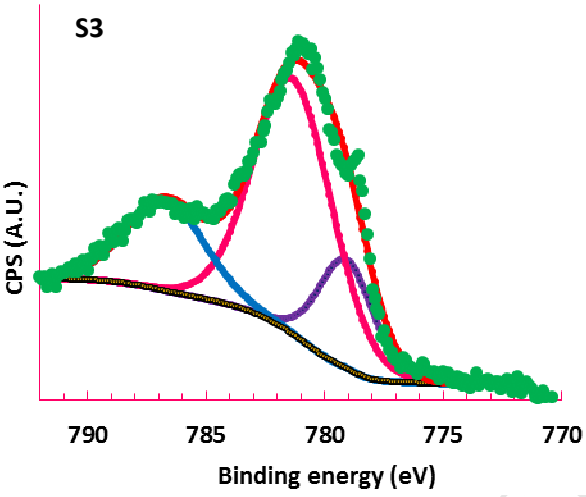
S3
CPS (A.U.)
790
785
780
775
770
Binding energy (eV)

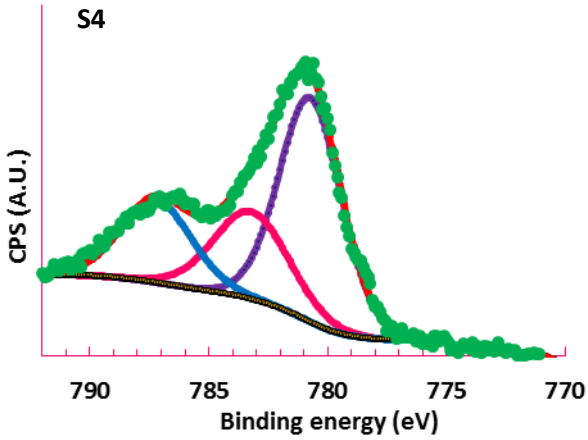
S4
CPS (A.U.)
790
785
780
775
770
Binding energy (eV)

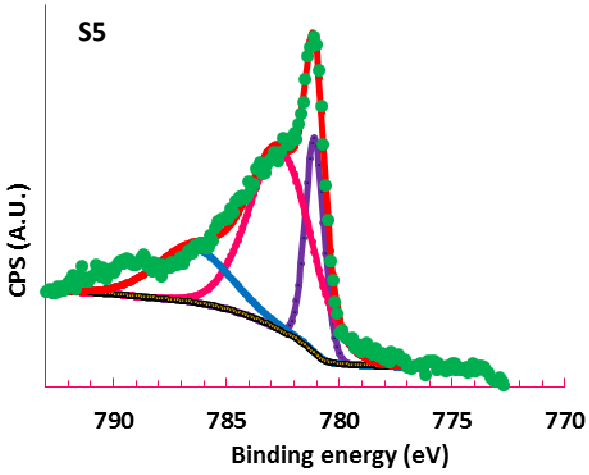
S5
CPS (A.U.)
790
785
780
775
770
Binding energy (eV)

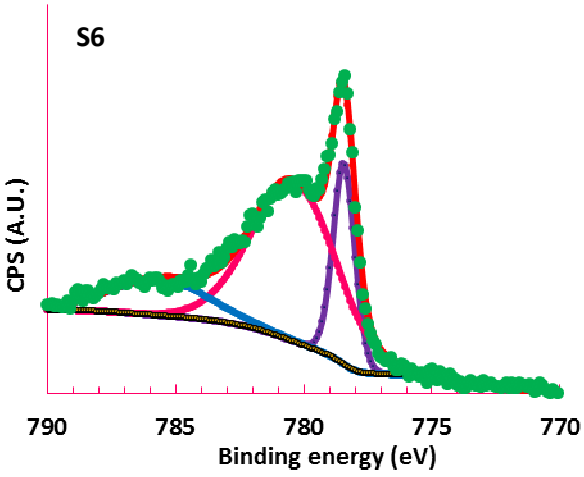
S6
CPS (A.U.)
790
785
780
775
770
Binding energy (eV)

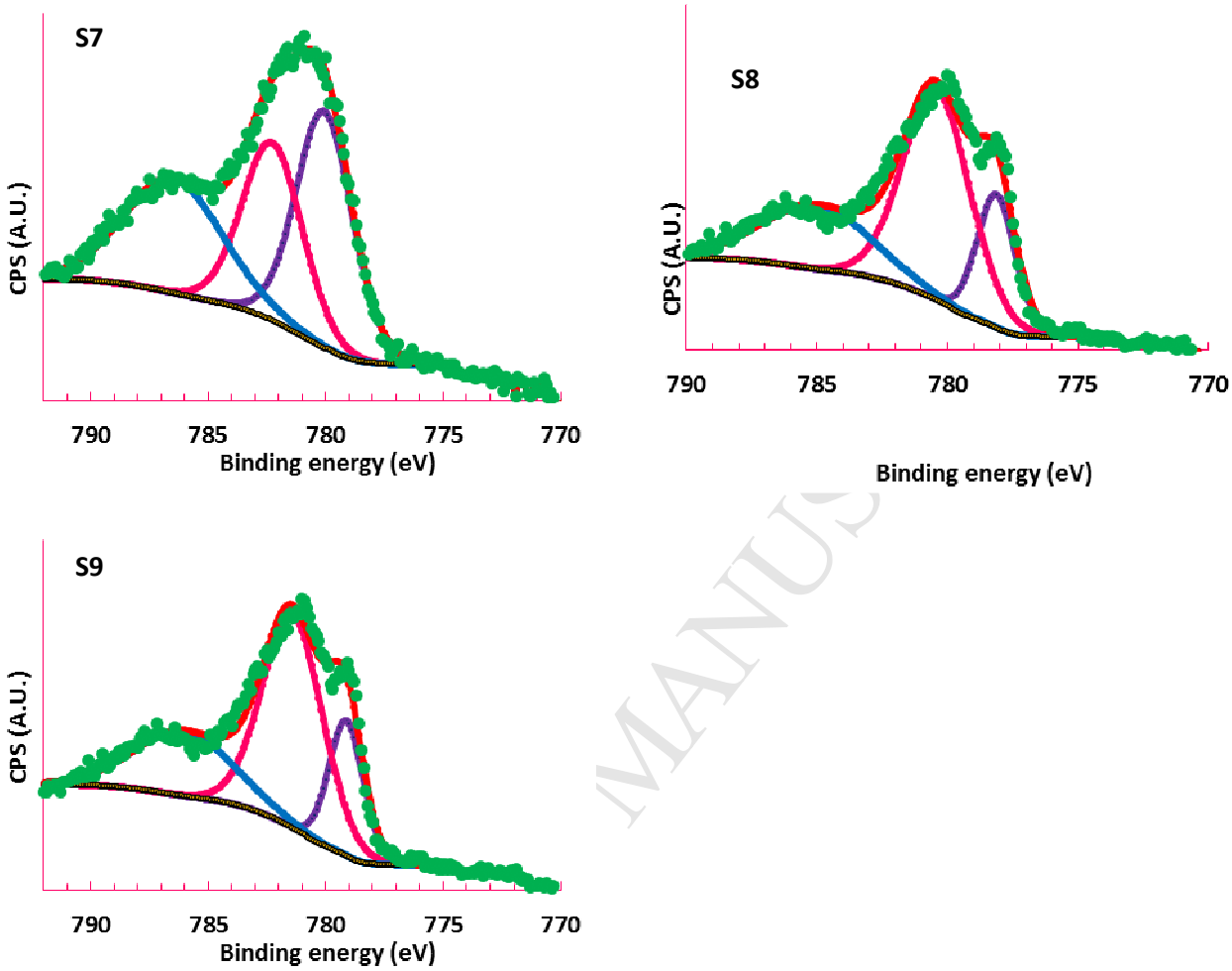

Figure 3. Deconvolution of high resolution XPS spectra of Co2$p_{3/2}$ photoelectron lines of sol-gel derived CoZnO thin film coatings. Green dotted line (raw data), red line (Fitting envelope), black line (background), purple, pink, and blue lines are fitting components.

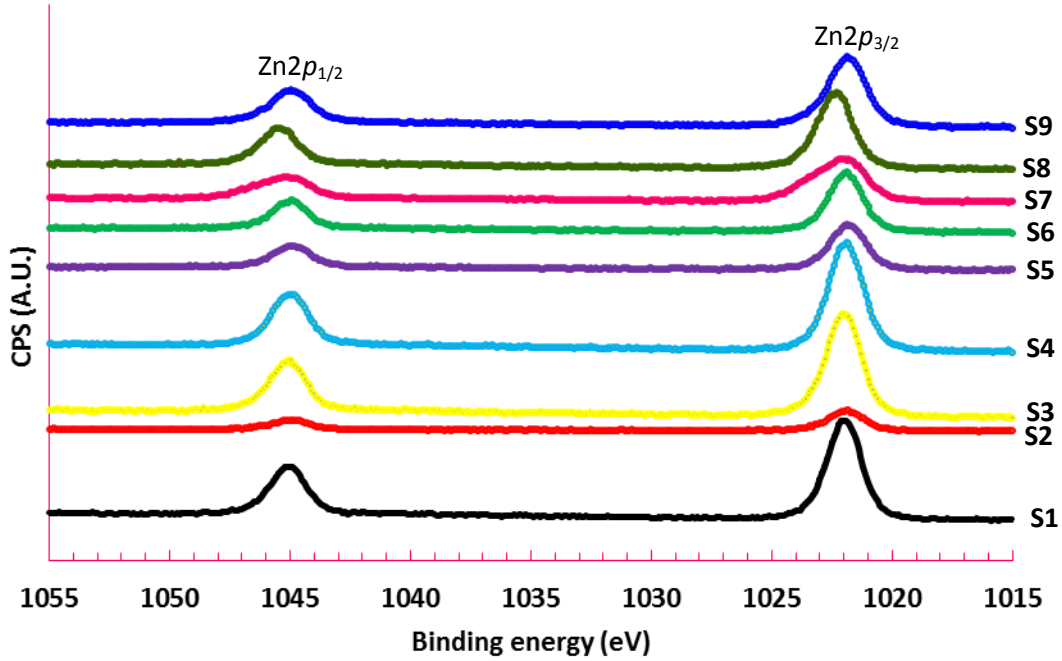

Figure 4. Zn2*p* photoelectron lines of the XPS spectra of sol-gel derived CoZnO thin film coatings before quantitative analysis.

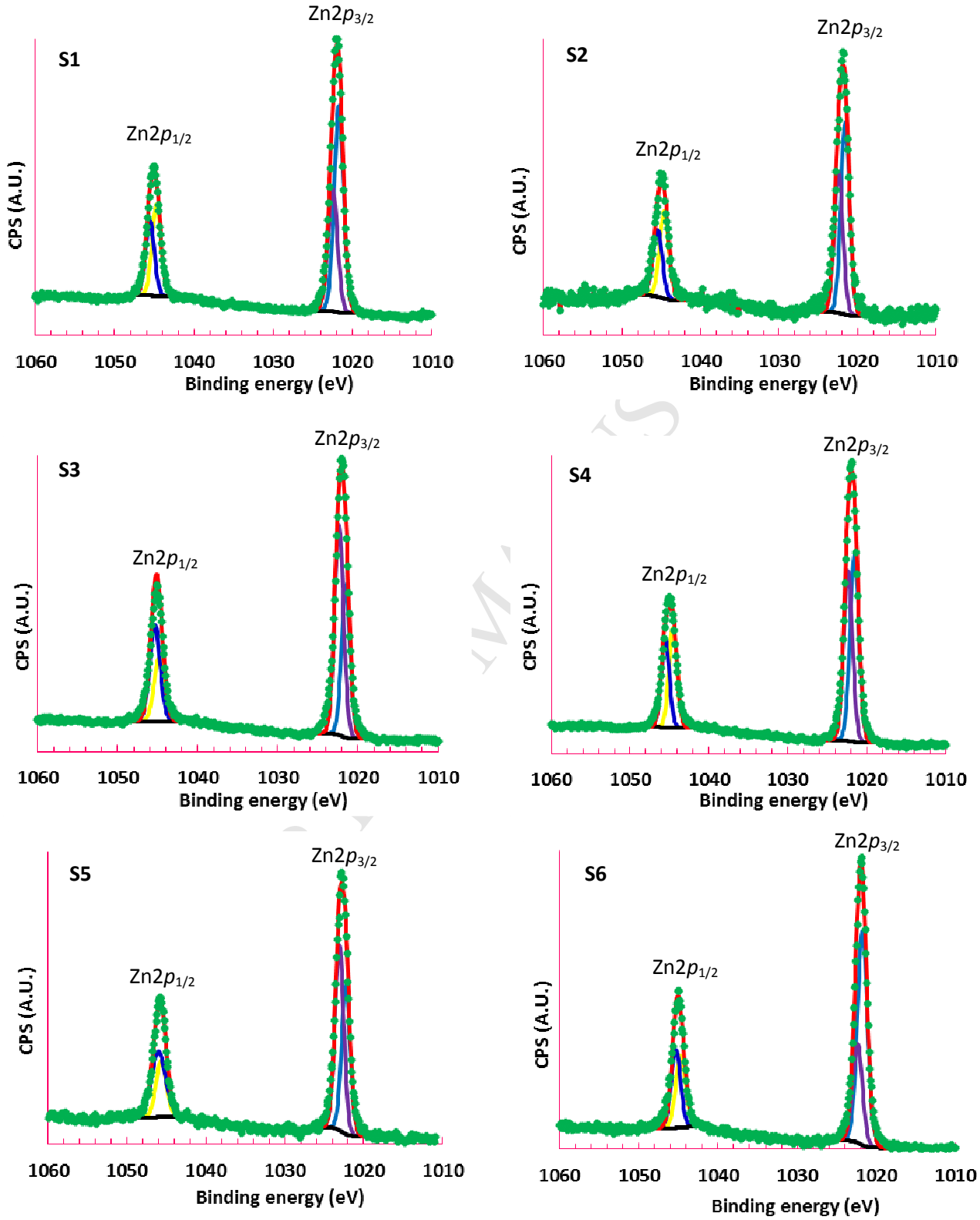
S1
Zn2$p_{3/2}$
Zn2$p_{1/2}$
CPS (A.U.)
1060 1050 1040 1030 1020 1010
Binding energy (eV)
S2
Zn2$p_{3/2}$
Zn2$p_{1/2}$
CPS (A.U.)
1060 1050 1040 1030 1020 1010
Binding energy (eV)
S3
Zn2$p_{3/2}$
Zn2$p_{1/2}$
CPS (A.U.)
1060 1050 1040 1030 1020 1010
Binding energy (eV)
S4
Zn2$p_{3/2}$
Zn2$p_{1/2}$
CPS (A.U.)
1060 1050 1040 1030 1020 1010
Binding energy (eV)
S5
Zn2$p_{3/2}$
Zn2$p_{1/2}$
CPS (A.U.)
1060 1050 1040 1030 1020 1010
Binding energy (eV)
S6
Zn2$p_{3/2}$
Zn2$p_{1/2}$
CPS (A.U.)
1060 1050 1040 1030 1020 1010
Binding energy (eV)

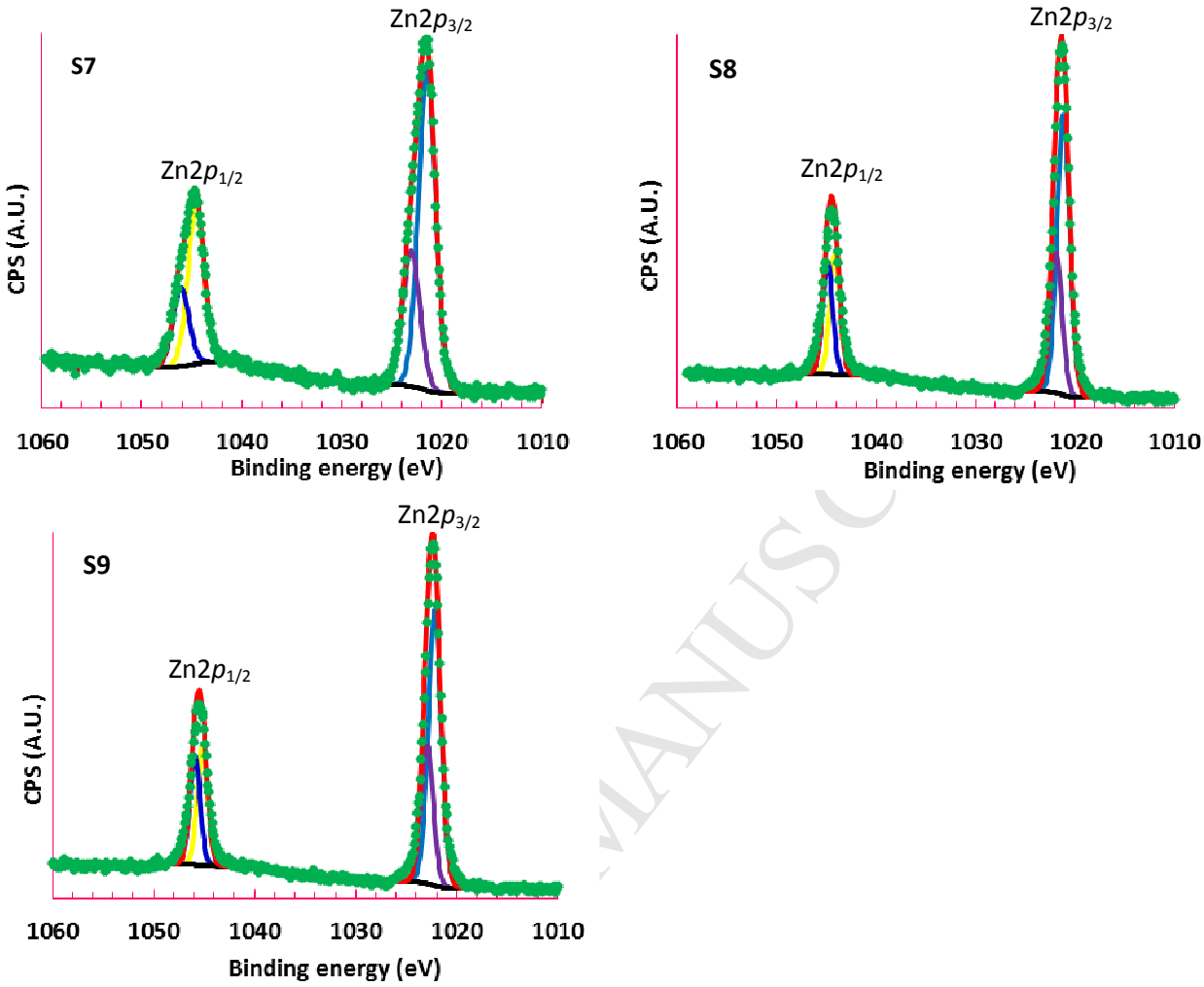

Figure 5. Deconvolution of high resolution XPS spectra of Zn2$p_{3/2}$ and Zn2$p_{1/2}$ photoelectron lines of sol-gel derived CoZnO thin film coatings. Green dotted line (raw data), red line (Fitting envelope), black line (background), purple, blue, dark blue, and orange lines are fitting components.

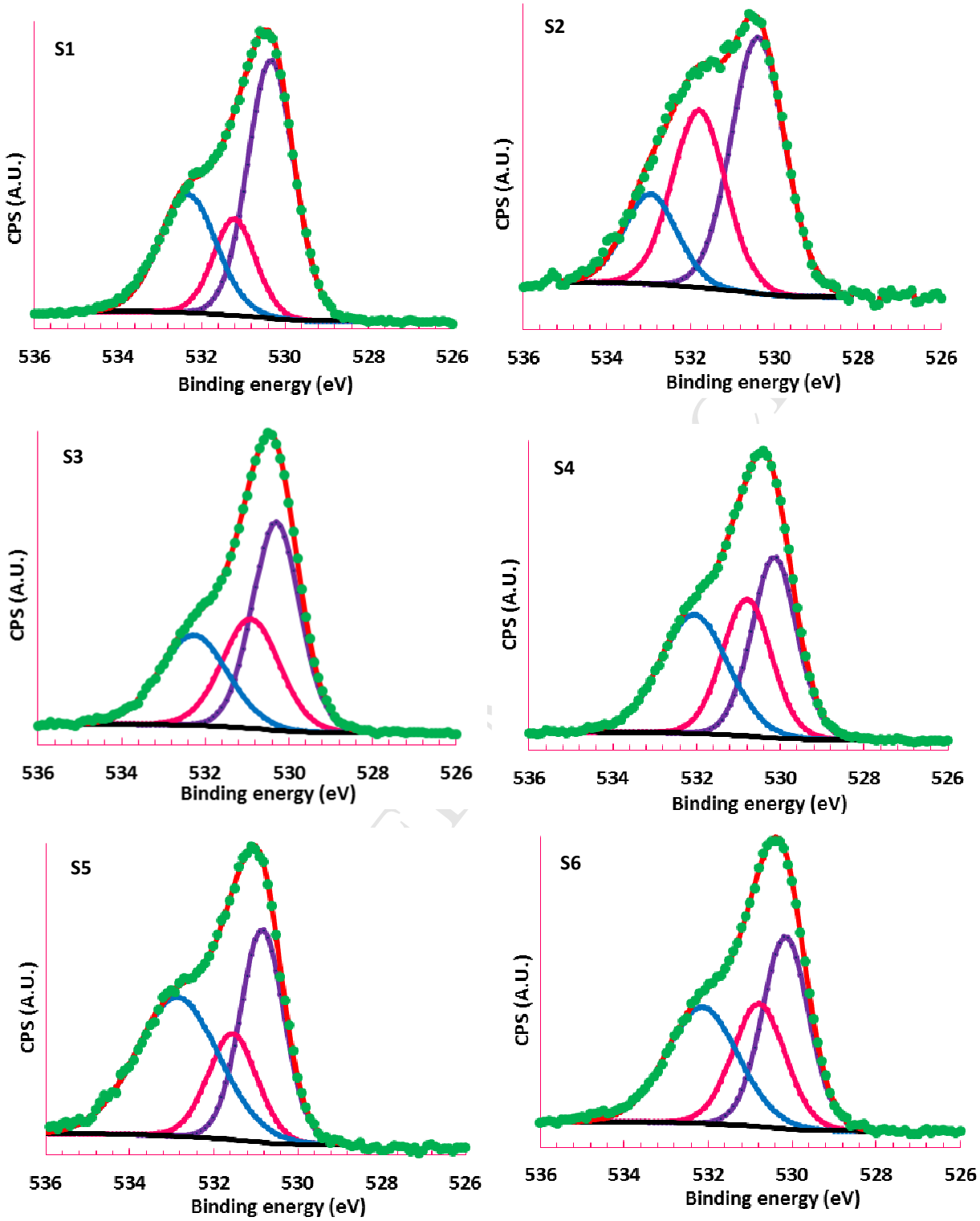

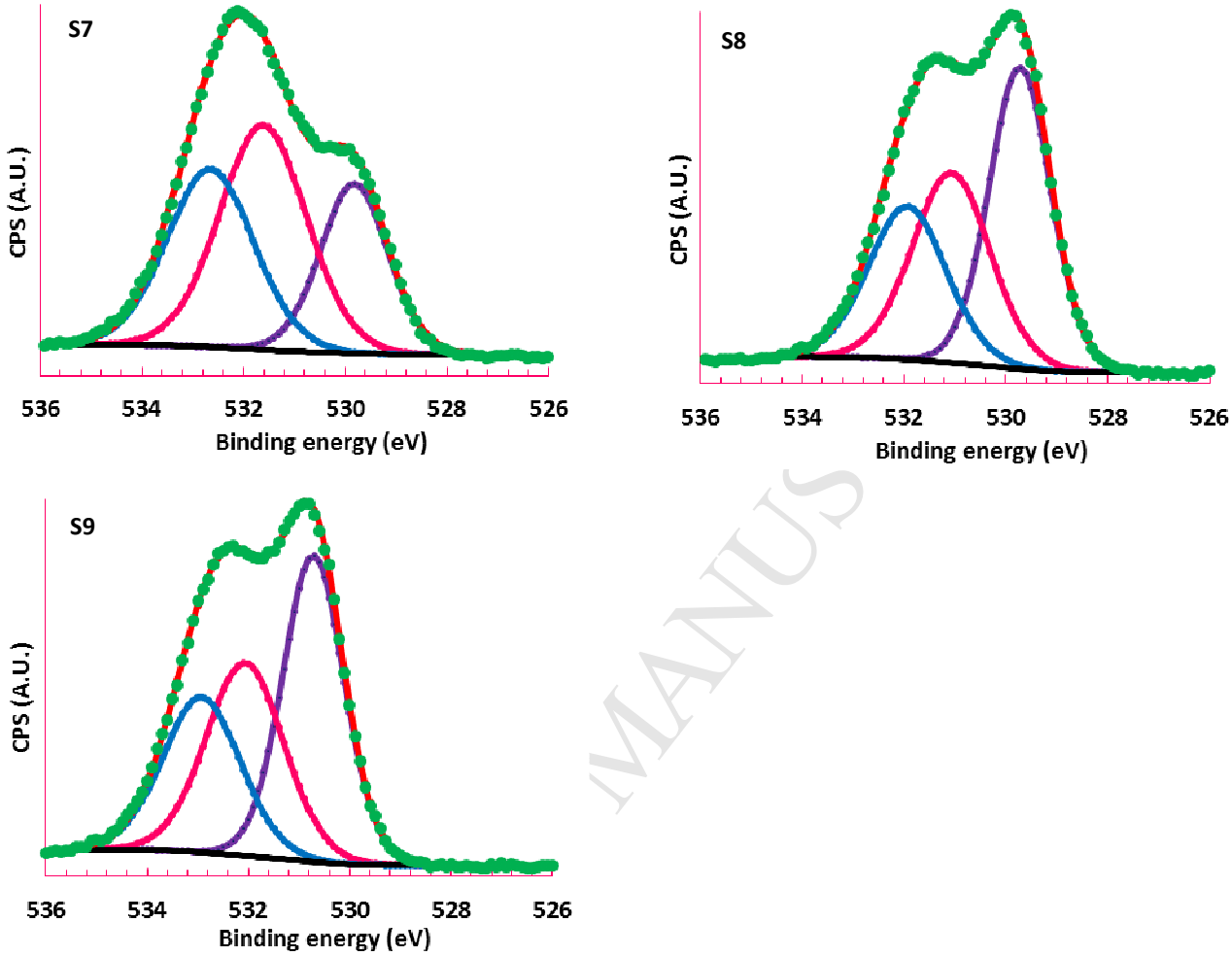

Figure 6. Deconvolution of high resolution XPS spectra of O1*s* photoelectron lines of sol-gel derived CoZnO thin film coatings. Green dotted line (raw data), red line (Fitting envelope), black line (background), purple, pink, and blue lines are fitting components.

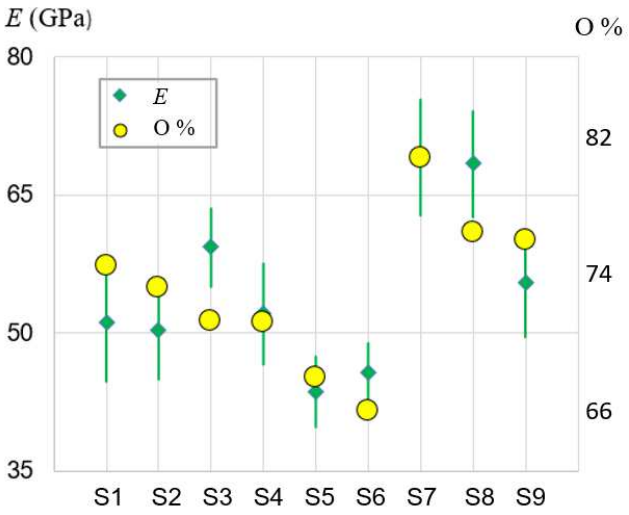

Figure 7. Experimental Young's modulus *E* of the CoZnO thin film coatings, derived from nanoindentation data. The percentage O content is also plotted for comparison, with the scale labelled on the right-hand side.

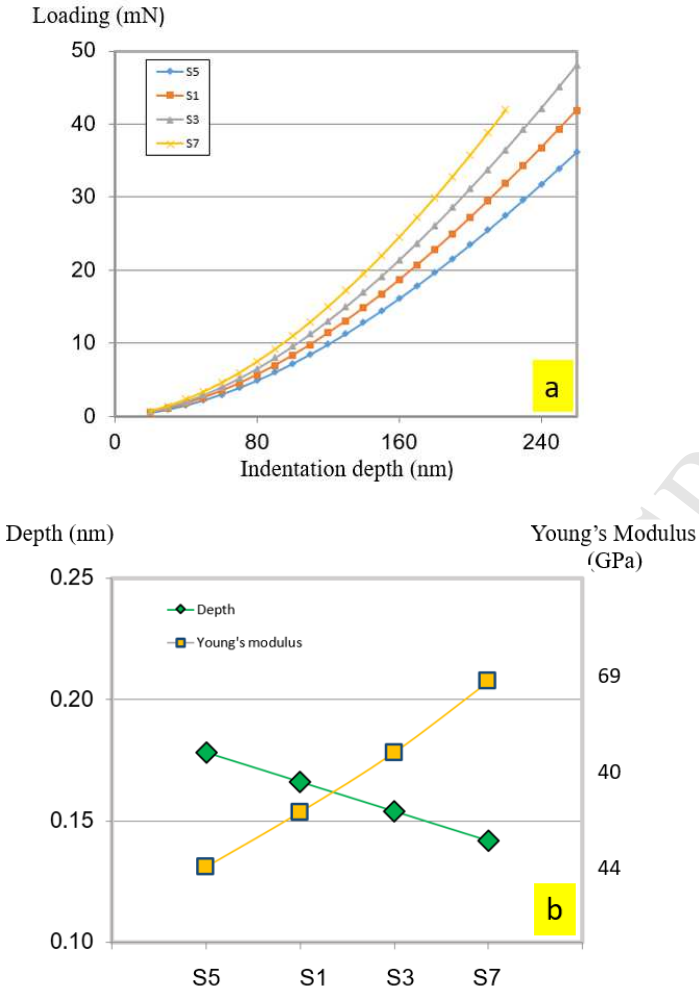

Figure 8. (a) FEM results of loading-depth plot for films S5, S1, S3 and S7. (b) FEM results of indentation depth at an indentation loading of 20 mN. The experimental Young's modulus is also shown for comparison.

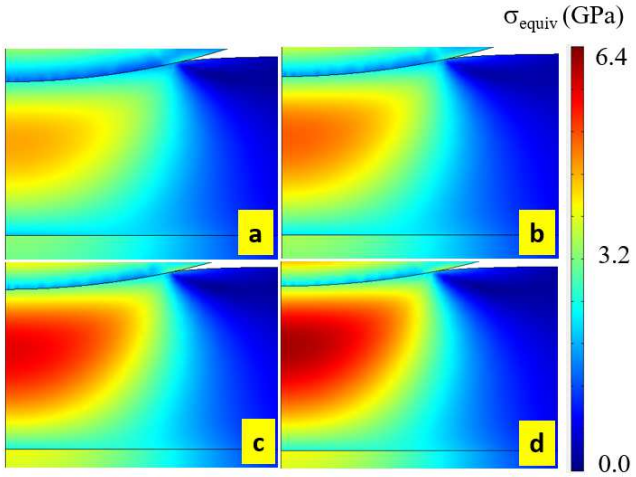

Figure 9. FEM modeling results of equivalent stress distribution within the films under an indentation loading of 20 mN. The thickness of the films is 1.2 μm, deposited on silicon substrates. (a) S5, (b) S1, (c) S3, and (d) S7. The indentation depth in S5 is 25% higher than that in S7 when subjecting to 20 mN loading.

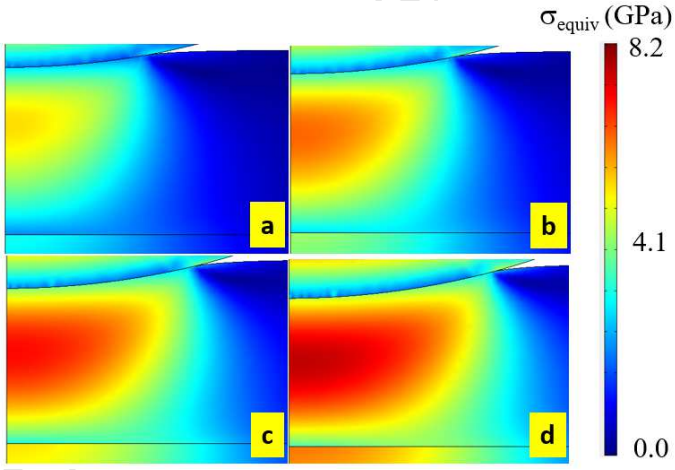

Figure 10. FEM modelling results of equivalent stress distribution within the film S7 with indentation depth, (a) 100 nm (b) 140 nm, (c) 280 nm, and (d) 220 nm. The thickness of the films is 1.2 μm, deposited on silicon substrates.

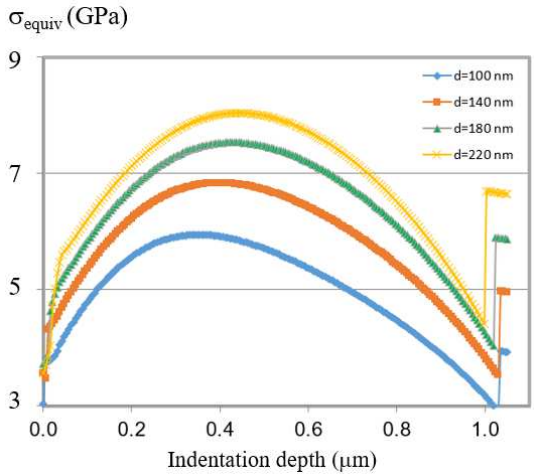

Figure 11. FEM modelling results of equivalent stress distribution in the film S8, along the symmetry axis of the model, from the top of the film to the film-substrate interface. The thickness of the films was 1.2 μm. The indentation depth is at (a) 100 nm, (b) 140 nm, (c) 180 nm, and (d) 200 nm.

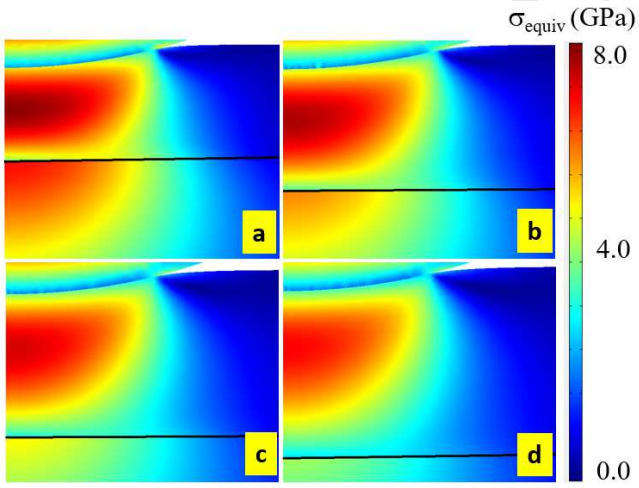

Figure 12. Modeling results of equivalent stress distribution within the S7 film, deposited on silica substrate with various thickness, (a) 1.0 μm, (b) 1.2 μm, (c) 1.4 μm, (d) 1.6 μm. A loading resulting in 0.22 μm indentation depth was used.

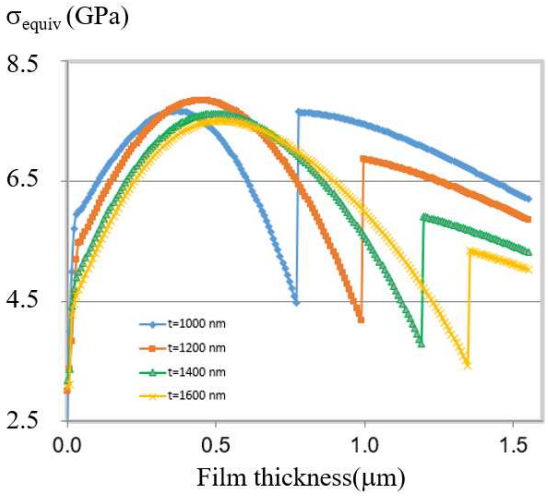

Figure 13. Equivalent stress distribution along the symmetry axis of the model, from the top of the film to the film-substrate interface. The film was deposited on silica substrate with various thickness, (a) 1.0 μm, (b) 1.2 μm, (c) 1.4 μm, and (d) 1.6 μm. A loading resulting in 0.22 indentation depth was applied.

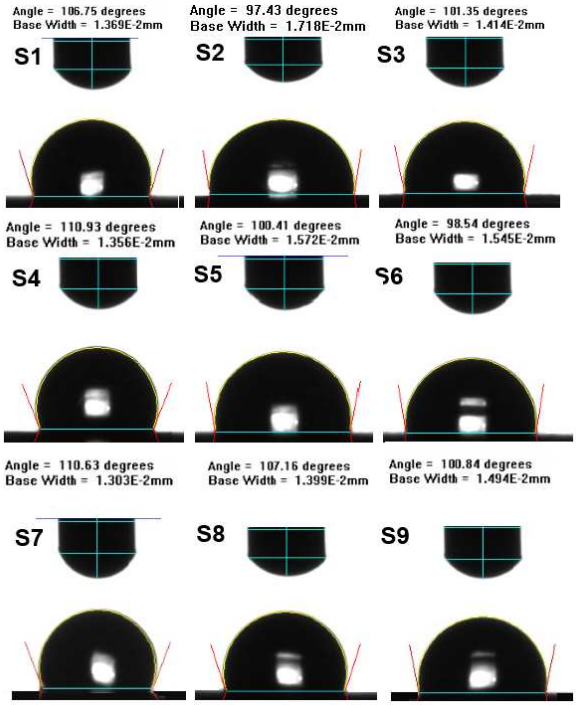

Figure 14. Experimental water contact angle images.

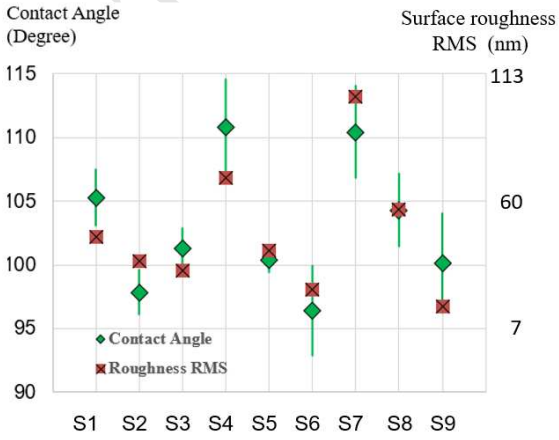

Figure 15. Experimental results of the water contact angles and surface roughness (RMS)